Inversion of coeval shear and normal stress of Piton de la Fournaise flank displacement

Marine Tridon, Valérie Cayol, Jean-Luc Froger, Aurélien Augier, Patrick Bachèlery

AGU PUBLICATIONS

JGR

Journal of Geophysical Research: Solid Earth

RESEARCH ARTICLE
10.1002/2016JB013330

Key Points:
- A new method for inverting displacement due to fractures submitted to coeval pressure and shear stress changes is presented
- The eastern flank displacement of Piton de la Fournaise is well explained by a shallow fracture undergoing closure and slip
- Thermal contraction of magma previously intruded in a coeruptive sill cannot explain the closure

Supporting Information:
- Supporting Information S1

Correspondence to:
M. Tridon,
m.tridon@opgc.fr

Citation:
Tridon, M., V. Cayol, J.-L. Froger, A. Augier, and P. Bachèlery (2016), Inversion of coeval shear and normal stress of Piton de la Fournaise flank displacement, *J. Geophys. Res. Solid Earth*, *121*, 7846–7866, doi:10.1002/2016JB013330.

Received 2 JUL 2016
Accepted 10 OCT 2016
Accepted article online 13 OCT 2016
Published online 11 NOV 2016

Inversion of coeval shear and normal stress of Piton de la Fournaise flank displacement

Marine Tridon[1], Valérie Cayol[1,2], Jean-Luc Froger[1], Aurélien Augier[1], and Patrick Bachèlery[1]

[1]Laboratoire Magmas et Volcans, Université Blaise Pascal–CNRS–IRD, OPGC, Aubière, France, [2]Université Jean Monnet, Université de Lyon, Saint-Etienne, France

Abstract The April 2007 eruption of Piton de la Fournaise was the biggest volcano eruptive crisis of the 20th and 21st centuries. Interferometric synthetic aperture radar (InSAR) captured a large coeruptive seaward displacement on the volcano's eastern flank, which continued for more than a year at a decreasing rate. Coeruptive uplift and posteruptive subsidence were also observed. While it is generally agreed that flank displacement is induced by fault slip, we suggest that this flank displacement might have been induced by a sheared sill, based on observations of sheared sills at Piton des Neiges. To test this hypothesis, we develop a new method to invert a quadrangular curved source submitted to simultaneous pressure and shear stress changes. This method, based on boundary elements, is applied to data acquired along six Envisat orbits covering a 14 month period subsequent to the April 2007 eruption. Posteruptive displacement is well explained by closure and slip of a large (5 km by 8 km) and shallow (500 m) trapezoidal fracture parallel to the flank and probably coincident with a lithological discontinuity. We investigate whether thermal contraction or degassing of a coeruptive sill can explain the displacement. Such a sill would have to be 10 times thicker than inferred from the coeruptive uplift and solidification time 10 times shorter (~20 days) than the duration of the posteruptive subsidence (24 to 33 months). Instead, we propose that the posteruptive eastern flank displacement is due to the compaction and ongoing slow slip on a shallow detachment fault.

1. Introduction

The morphology of volcanoes changes continuously in response to the accumulation of lava flows and to the surface deformation generated by intrusions and tectonic activity. One of the greatest hazards associated with these changes is the magma induced destabilization of volcano flanks by slip along faults, often located at a lithological discontinuity. At Kilauea Volcano in Hawaii (USA), an 8 km deep décollement-type fault has been identified beneath the southeastern flank [*Zucca and Hill*, 1980; *Syracuse et al*., 2010] at the interface between the sea floor and the volcanic edifice. Continuous rift zone inflation, induced by shallow magma intrusions and deep creep of a cumulate-rich melt [*Plattner et al*., 2013; *Montgomery-Brown et al*., 2015] is accommodated by fault slip, generating continuous seaward flank motion [*Delaney et al*., 1990; *Dieterich et al*., 2000; *Owen et al*., 2000] along with recurrent strong earthquakes [*Ando*, 1979; *Arnadottir and Segall*, 1991] and slow slip events [*Montgomery-Brown et al*., 2015]. At Mount Etna (Italy), a normal fault with a low-dip angle to the east at a depth of 1 to 3 km has been proposed to explain the frequent seaward displacement of the eastern flank [*Bonforte and Puglisi*, 2003; *Lundgren et al*., 2003; *Puglisi et al*., 2008; *Bonaccorso et al*., 2013]. This depth corresponds to a presumed clay layer trapped between the sedimentary basement and the volcanic edifice [*Cianetti et al*., 2012]. *Puglisi et al*. [2008] highlighted that slip increases when intrusions occur near the summit. At Cumbre Vieja Volcano (La Palma, Canary Islands), the western flank subsidence observed during intereruptive periods has been modeled by a 2 to 4 km deep detachment fault [*Gonzalez et al*., 2010]. At Stromboli, the source of the seaward slip of the northeastern flank is a very shallow (~200 m deep) planar fracture with a high dip angle subparallel to the topography, which may match the dip angle of sequences of lava flows constituting the flank [*Baldi et al*., 2008; *Di Traglia et al*., 2014]. Slip accelerations are correlated with eruptive activity [*Intrieri et al*., 2013; *Nolesini et al*., 2013].

An alternative process for flank destabilization has been indicated by field investigations at Piton des Neiges, the extinct volcano of La Réunion Island (Figure 1a). The existence of a large discontinuity associated with a stack of low-dip intrusions presenting ductile and brittle deformation has been interpreted as a detachment plane [*Famin and Michon*, 2010; *Berthod et al*., 2016]. Injections of magma along this plane of weakness can trigger cointrusive lateral displacement of the volcano flanks, in the form of sheared sills. Indeed, when the injection of magma is guided by a preexisting discontinuity rather than the minimum principal stress, the

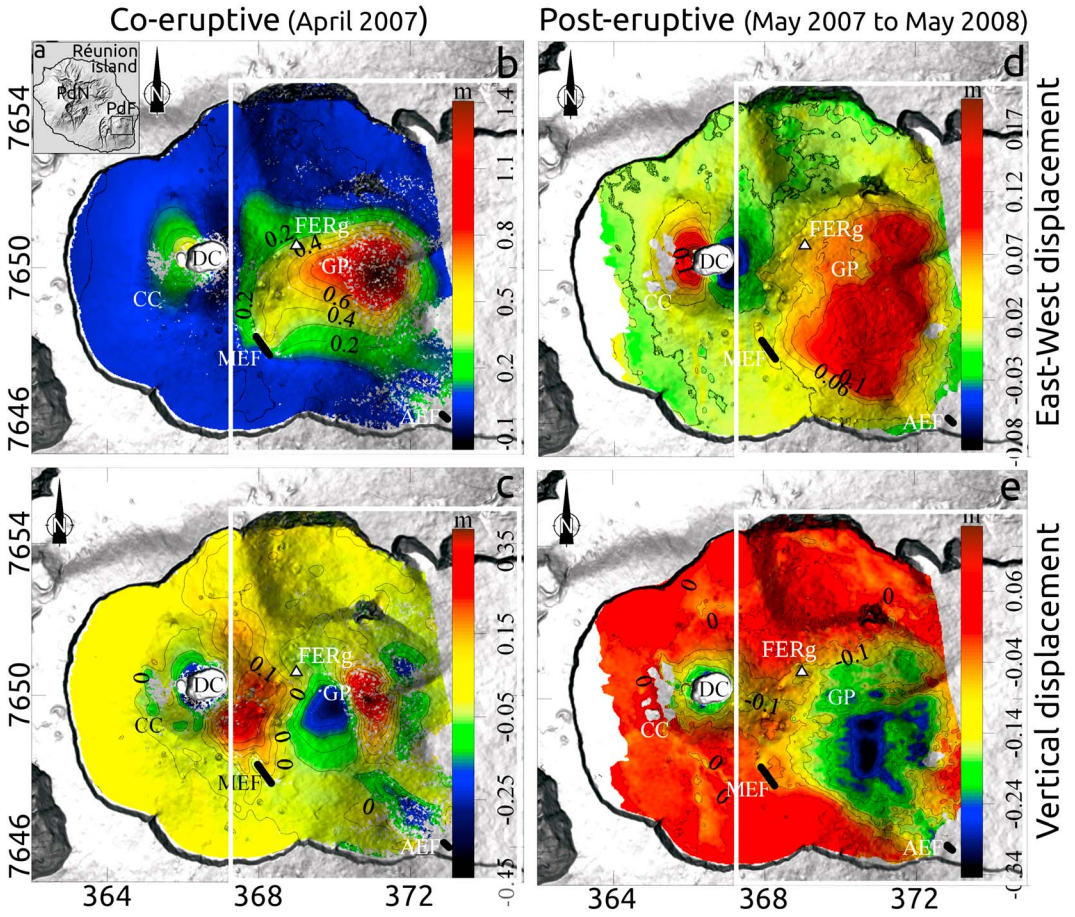

Figure 1. (a) Location of the active Piton de la Fournaise (PdF) and the extinct Piton des Neiges (PdN) Volcanoes on La Réunion Island. (b, c) East-west and vertical displacement for the coeruptive period (April 2007). (d, e) East-west and vertical displacement for the posteruptive period (May 2007 to May 2008). Thick black lines indicate the location of Eruptive Fissures from March and April (MEF and AEF, respectively); the white triangle is the FERg GPS station; CC: Central Cone; DC: Dolomieu Crater; GP: Grandes Pentes; the white rectangle outlines the region shown in Figures 6a–6e. Coordinates correspond to UTM WGS84 (zone 40S).

resulting fracture is submitted not only to overpressure but also to tangential stress. When the volcano stress field resulting from gravity is extensive, simultaneous cointrusive flank displacement and fracture opening are induced [*Cayol et al*., 2014; *Chaput et al*., 2014a]. Following this approach, *Chaput et al*. [2014b] proposed a new model for flank failure of basaltic volcanoes in which cycles of stress permutations explain the variety of stress fields, as inferred from detailed microstructural studies at Piton des Neiges. Each cycle starts with dike intrusions in an extensional stress field, continues with intrusions of sheared sills acting as detachment planes, and finishes with the restoration of the extensional stress field allowing new dike intrusions. Considering the similarity between Piton des Neiges and Piton de la Fournaise, *Chaput et al*. [2014a, 2014b] proposed that this cointrusive lateral flank displacement model could also apply to the April 2007 eruption of Piton de la Fournaise (Figure 1a). Indeed, a large 1.4 m seaward movement of the eastern flank of the Piton de la Fournaise Volcano, with a simultaneous 35 cm uplift, was observed with interferometric synthetic aperture radar (InSAR) during the major April 2007 eruption. As flank movement is consistent with debris avalanche deposits observed offshore of Piton de la Fournaise [*Labazuy*, 1996; *Oehler*, 2005; *Le Friant et al*., 2011], it raises the importance of understanding the origin of such events to better anticipate the occurrence of catastrophic flank collapses.

To decipher which process of flank destabilization, i.e., slip on faults or intrusion of sheared sills, is occurring, it is important to take both the opening and slip into account. In this paper, we propose a new method to simultaneously invert stresses which are normal and tangential to fractures, along with their geometry and

location. Our stress inversion has several advantages over displacement (or kinematic) inversions, traditionally used for intrusions and faults. First, we invert shear and normal stresses simultaneously, which is mechanically relevant since several observations attest that magma sometimes intrudes along preexisting faults [*Delaney*, 1986; *Rossetti et al*., 2000; *Valentine and Krogh*, 2006; *Famin and Michon*, 2010; *Spacapan et al*., 2016], a process attributed to the reduced strength of fractures favorably oriented with respect to the stress field [*Delaney*, 1986; *Ziv et al*., 2000]. However, with the exception of studies by *Hooper et al*. [2011] and *Sigmundsson et al*. [2015] which used displacement inversions, shear and normal components are always inverted separately. Second, our inversions rely on stress solutions, which are physically more realistic than displacement solutions. Stress boundary conditions agree with the physics of intrusions, where hydraulic connectivity results in homogeneous pressure. Stress boundary conditions inherently lead to smooth displacement over the fracture [*Zeller and Pollard*, 1992], whereas displacement solutions require a smoothness constraint to regularize the inversion and obtain smooth solutions [*Harris and Segall*, 1987]. Third, given the fracture geometry, our inversion requires less parameters than displacement inversions. By imposing uniform stress, a single parameter is required for fracture displacement [*Fukushima et al*., 2005; *Sun et al*., 2011], whereas displacement inversions require as many parameters as there are fracture elements. Finally, we simultaneously invert for fracture, stress, geometry, and location, whereas most inversions invert for geometry and location before inverting for fracture displacement or stress. In the latter process the optimal solution might be missed as fracture stresses are not independent of the geometry and location. Following *Fukushima et al*. [2005] or *Sun et al*. [2011], we determine the fracture stress change for each fracture model tested in the inversion.

The April 2007 eruption is characterized by the largest emitted volume of lava of the 20th and 21st centuries (240×10^6 m^3 [*Roult et al*., 2012]) and two remarkable volcano-tectonic events. The first is the 340 m high summit caldera collapse [*Michon et al*., 2007a; *Peltier et al*., 2007], and the second is a large (up to 1.4 m) seaward movement of the eastern flank of Piton de la Fournaise, which is the subject of this study. Coeruptive displacement, evidenced by InSAR [*Froger et al*., 2015], shows a complex pattern resulting from at least three different sources (Figures 1b and 1c). The western part of the Central Cone is affected by centripetal subsidence, corresponding to the summit caldera collapse, whereas the eastern part shows a large inflation axis with asymmetric horizontal displacement, corresponding to the intrusion of a north–south oriented dyke. Major downslope displacement of up to 1.4 m visible on the eastern flank of the edifice, in the area of the Grandes Pentes, coincident with a 45 cm inflation, corresponds to a fracture movement. Posteruptive displacement covering a one year period after the eruption (from May 2007 to May 2008) is simpler (Figures 1d and 1e) and attests to the ongoing deformation of two of the coeruptive sources. The Central Cone still shows centripetal subsidence and the eastern flank continues to move at rates of up to 15 cm/yr and 34 cm/yr eastward and downward, respectively. Both displacements decay exponentially with time (Figure 8). Because the posteruptive displacement is simpler than the coeruptive one, we invert the posteruptive displacement to infer the source of the eastern flank displacement.

This paper investigates flank displacement associated with the April 2007 eruption through a simultaneous inversion of the shear and normal stress changes which induced the posteruptive displacements. Section 2 details the April 2007 eruption. Section 3 describes the method for the simultaneous inversion of the normal and shear stress changes, and the methods for fracture displacement inversion. In section 4, the Envisat-ASAR (advanced synthetic aperture radar) data processing and their subsampling are explained. Section 5 compares results for fractures with increasing complexities and the Akaike information criteria is used to estimate the most likely model. All models, regardless of their complexity, point to closure of a shallow low-angle surface. Finally, section 6 explores explanations for the fracture closure and downslope slip.

2. The April 2007 Eruption of Piton de la Fournaise

The Piton de la Fournaise volcano is the youngest of the three edifices which make up La Réunion Island (Figure 1a), located 700 km east of Madagascar in the Indian Ocean. This basaltic shield volcano is one of the world's most active volcanoes with the occurrence of about 60 eruptions during the last 30 years. Most eruptions, classified as summit or proximal eruptions [*Peltier et al*., 2008], are characterized by eruptive fissures located within the summit crater (Dolomieu crater) or on the flanks of the Central Cone of the volcano, and poorly phyric lavas [*Boivin and Bachèlery*, 2009; *Peltier et al*., 2009b]. The associated deformation signals

are well explained by dykes, with uplift and horizontal displacement away from the eruptive fissures [*Froger et al*., 2004; *Fukushima et al*., 2005, 2010; *Peltier et al*., 2008]. These eruptions alternate with so-called distal eruptions [*Peltier et al*., 2008] which regularly occur at a greater distance from the summit. Distal eruptions are associated with large volumes of olivine-rich lavas [*Boivin and Bachèlery*, 2009; *Peltier et al*., 2009b], and the deformation signal cannot be modeled by dykes [*Tinard*, 2007].

The April 2007 eruption is a distal eruption which followed three summit eruptions (July to August 2006, August 2006 to January 2007 and February 2007). The first phase of the eruption was characterized by the opening of a fissure on 30 March at 1900 m above sea level at the southeastern base of the Central Cone (Figure 1). Lava effusion lasted about 10 h and fed a small lava flow ($<10^6$ m^3) of aphyric basalt [*Staudacher et al*., 2009]. The displacement observed during this phase was interpreted as the intrusion of a north–south oriented dyke [*Froger et al*., 2015]. On 2 April, a second eruptive fissure, also emitting aphyric basalt, opened 7 km away from the summit on the lower eastern flank at ~600 m above sea level (Figure 1). This second phase is remarkable in several respects.

1. It is characterized by the largest emitted volume of lava of the 20th and 21st centuries (240×10^6 m^3 [*Roult et al*., 2012]).
2. The large effusion of magma resulted in a 340 m high summit caldera collapse. The collapse occurred on 5 and 6 April, simultaneously with an increase in seismic activity beneath the Central Cone, 200 m high lava fountains [*Michon et al*., 2007b; *Peltier et al*., 2009a; *Staudacher et al*., 2009] and a strong rise in the olivine content of the lava [*Di Muro et al*., 2014], indicating a strong connection between the central zone of the volcano and the plumbing system of the April eruptive fissure.
3. The eruption was coincident with a large seaward movement of the eastern flank of Piton de la Fournaise first revealed here by InSAR.

Froger et al. [2015] computed east–west and vertical components of displacement for coeruptive and poster-uptive periods from six ASAR and PALSAR interferograms (Figures 1b–1e), which indicate that the largest displacement was recorded before 20 April. It reached 1.4 m eastward and was associated with a 45 cm subsidence to the east and a 35 cm uplift to the west (Figures 1b and 1c). Geodetic and petrological studies of the April 2007 eruption suggest two possible mechanisms for the flank displacement. Some studies favor a sill model. The GPS station FERg, which was the only station on the eastern flank in 2007 (see Figure 1 for location), showed upward displacement at 16:25 on 30 March before showing eastward displacement at 16:30. *Got et al*. [2013] interpreted this displacement as the onset of the intrusion of a sill below FERg and related the eastward displacement at FERg to slip of the Grandes Pentes. At 16:38 the summit stations detected a contraction of the Central Cone, indicating the beginning of the magma transfer toward the 30 March eruptive fissure. The 30 March dyke intrusion would therefore be a consequence of the onset of the slip of the Grandes Pentes: eastward flank slip decreased the east–west stress close to the summit making it the minimum principal stress, further enabling a north–south dyke intrusion [*Froger et al*., 2015]. The nature of the products of the April 2007 eruption, i.e., olivine-rich basalts, is also consistent with the hypothesis of a sill. Indeed, olivine-rich magmas come from the base of the reservoir where crystals accumulate [*Famin et al*., 2009]. Moreover, finite element models of magma reservoirs [*Grosfils*, 2007] show that when tensile failure occurs at the midpoint of reservoirs, it promotes the injection of magma along sills. Furthermore, *Di Muro et al*. [2014] found moderate volatile content in the melt inclusions of olivines from April 2007, which indicates low-pressure crystallization. They proposed that the April 2007 magmas crystallized at pressures between 18 and 34 MPa, which corresponds to depths of 500 to 1800 m, assuming lithostatic stresses. The hypothesis of a shallow magma storage zone is also supported by the anomalous depletion in Li, Cu, and Tl observed in the first lavas erupted on 2 April [*Vlastélic et al*., 2013]. *Froger et al*. [2015] proposed that this storage zone could be situated in the central part of the eastern flank (Figure 1c). An alternative analysis favors a fault model. *Cayol et al*. [2014] formulate a decision tree to determine fracture characteristics and the host rock stress anisotropy from the ratios of maximum observed surface displacement. Applying the decision tree to the coeruptive flank deformation of April 2007, they found that it probably originated from a shallow-depth eastward dipping subhorizontal normal fault rather than a sheared intrusion. However, the observed displacement ratios were not fully explained by the model, so they suggested that the model might be too simple or that the displacement might contain other contributions, i.e., the 30 March dyke intrusion and the caldera collapse.

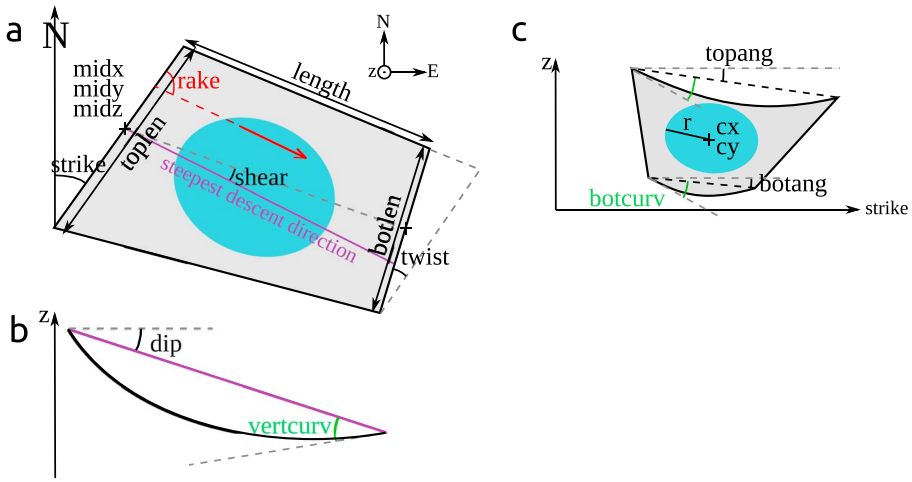

Figure 2. Representation of the 18 parameters that are used to model a quadrangular fracture subjected to pressure and shear stress changes on a circular patch. (a) Top view. Length, botlen, toplen, shear, and rake are defined in the fracture plane. The blue circular patch is submitted to pressure and shear stress changes whose direction (the rake) is represented by the red vector. For simplicity, the curvature is not represented here. (b) Vertical view perpendicular to the steepest descent direction in purple. (c) Vertical view perpendicular to the strike of the fracture. See Table 1 for a description of the parameters.

3. Inverse Modeling Methods

The ground deformation is linearly related to the slip or opening distribution on a fracture and nonlinearly to the fracture location and geometry. We combine a boundary element forward model and a neighborhood inversion algorithm for the nonlinear inversion of the fracture location, geometry [*Fukushima et al*., 2005] and area of pressure, and shear stress change, which is assumed to be circular. We also use this fault geometry and location to conduct a linear inversion of the displacement distribution using the solution of *Meade* [2007].

3.1. Nonlinear Inversion of the Geometry and Location

3.1.1. The 3-D Mixed Boundary Element Method

Ground displacement is computed using a 3-D Mixed Boundary Element Method (later called MBEM) [*Cayol and Cornet*, 1997] which combines two boundary element methods. The direct method is the most efficient for modeling pressurized reservoirs and the discontinuity method is numerically stable for fractures. The edifice is assumed to be linearly elastic, homogeneous, and isotropic, with a Young's Modulus of 5 GPa and a Poisson's ratio of 0.25, as proposed by *Fukushima et al*. [2005]. The method also takes topography into account, which can be important in the case of volcanoes where the slopes are generally steep.

Applicability and precision of MBEM for the modeling of volcano deformations have been tested [*Cayol and Cornet*, 1997; *Fukushima et al*., 2005] and the method has proved its effectiveness on several targets. Inflation coupled with divergent displacement, typical of dyke intrusions, have been modeled by fractures submitted to overpressure for several summit events at Piton de la Fournaise Volcano [*Cayol and Cornet*, 1998; *Froger et al*., 2004; *Fukushima et al*., 2005, 2010; *Peltier et al*., 2007, 2008], at Nyamulagira and Nyiragongo volcanoes, Democratic Republic of the Congo [*Wauthier et al*., 2012, 2013], at Mount Merapi, Indonesia [*Beauducel and Cornet*, 1999], at Etna Volcano, Italy [*Beauducel and Carbone*, 2015], and at Kilauea Volcano, Hawaii, USA [*Cayol et al*., 2000].

The construction of the topographic mesh is detailed in Text S1 in the supporting information. The posteruptive displacement is close to the eastern coast of La Réunion Island, thus the submarine topography is taken into account in the modeling (Figure S1 in the supporting information). Indeed, comparing computed displacement with the submarine topography and considering the ground surface is at sea level, shows that a 5 mm RMS (root-mean-square) error is induced when the bathymetry is not considered.

The source is assumed to be a quadrangle submitted to pressure and shear stress changes. In practice, the linearity of the mechanical problem is taken into account and two stress conditions on the same source

Table 1. Definition of the 18 Parameters That Are Used to Model a Quadrangle Subjected to Pressure and Shear Stress Changes in the Mixed Boundary Element Modeling

Parameter Name	Description
Midx, Midy and Midz	*x*, *y*, and *z* coordinates of the midpoint of the top side of the quadrangle
Toplen	length of the top side
Topang	vertical angle of the top side measured from horizontal
Strike	horizontal angle of the top side measured from north direction
Dip	dip angle of the quadrangle
Shear	angle between the steepest descent direction and the line connecting the midpoints of the top and bottom sides
Length	distance between top and bottom midpoints
Twist	horizontal angle between top and bottom sides measured clockwise
Botlen	length of the bottom side
Botang	vertical angle of the bottom side measured from horizontal
Botcurv	along-strike curvature
Vertcurv	along-dip curvature
Cx and Cy	*x* and *y* coordinates of the center of the circular stress patch
R	radius of the circular stress patch
Rake	angle of shear displacement measured from the strike direction in the fault plane

are simulated, one where the source is submitted to a pressure change and the other where the source is submitted to a shear stress change. The computed surface displacement of each solution are then summed. The quadrangular fracture is defined by up to 14 geometrical parameters which allow for complex quadrangles, with angles between their sides and curvature along their strike and dip (Figure 2 and Table 1). Using displacement solutions, the opening distribution of intrusions [*Amelung et al*., 2000; *Desmarais and Segall*, 2007; *Montgomery-Brown et al*., 2010] or the slip distribution of faults [*Jonsson et al*., 2002; *Sun et al*., 2011; *Fukushima et al*., 2013] is often found to be of a roughly circular shape (close to an ellipse). Based on this, a nonnull homogeneous stress change is applied to a circular patch and null stress to the rest of the fracture which can thus move passively. Only four parameters are necessary to define the geometry of the circular patch and the slip direction, resulting in a maximum of 18 parameters to define the fracture geometry. The optimal amplitudes of the normal and shear stress changes are determined for each forward model, by taking advantage of the linearity of the mechanical problem as explained in the following section.

A model needs at least nine parameters (midx, midy, midz, toplen, strike, dip, length, botlen, and rake; Figure 2 and Table 1) in order to be computed, the others being optional and only used to make the geometry and stress inversion more complex. As the rake is defined from the strike direction, there is a strong tradeoff between these two parameters, such that they cannot be independently inverted, and either the strike or the rake has to be fixed. Because InSAR data are acquired from satellites on Polar orbits, they poorly resolve the north component of displacement. Thus, the rake is fixed at 90° based on the eastward GPS displacement recorded between 2 and 10 April at the only station (FERg) located to the east of the summit [*Peltier et al*., 2009a]. We also use a modified computation where fracture interpenetration is not permitted, a condition enforced through the use of Lagrange multipliers as explained in *Cayol et al*. [2014]

3.1.2. Nonlinear Inversion With a Neighborhood Algorithm

Following *Fukushima et al*. [2005], forward mixed boundary element computations are combined with a Monte Carlo Neighborhood Algorithm (NAMBEM) where the vicinity of a model in the parameter space is defined by Voronoï tessellation. The inversion consists of two stages: a search and an appraisal stage.

The search stage [*Sambridge*, 1999a] consists of looking for the model parameters that best explain the observed data. At the first iteration, the number of models randomly drawn from the parameter space is an exponential function of the number of inverted parameters, k ($9.775 \times e^{(0.457 \times k)}$ from Figure 5 in *Sambridge* [1998]). For subsequent iterations, following *Fukushima et al*. [2005], the n models with the lowest misfits are selected and n new random models are generated in their vicinity. Following *Fukushima et al*. [2005], $n = 30$. The algorithm stops when the mean standard deviation on the model parameters reaches less

than 0.3%. For each model, the discrepancy between observed and modeled data is evaluated by calculating the least squares misfit function as follows:

$$\chi^2(m) = \|\boldsymbol{W}\boldsymbol{u_r}\|_2 \tag{1}$$

where $\boldsymbol{u_r} = \boldsymbol{u_o} - \boldsymbol{u_m}$ is the residual displacement between observed and modeled displacement, $\boldsymbol{u_o}$ is composed of subsampled interferometric displacement with different imaging geometries, and $\boldsymbol{u_m}$ is obtained by multiplying the modeled displacement vectors by the line-of-sight vector of each interferogram. Interferogram filtering and subsampling is explained below in section 4. $\boldsymbol{W}$ is the inverse of the Cholesky decomposition of the data variance-covariance matrix $\boldsymbol{C_d^{-1}} = \boldsymbol{W^T W}$, constructed from an autocorrelation function determined from the correlated atmospheric noise of InSAR data, which can be approximated by an exponential correlation function $C(r) = \sigma_d^2 * \exp(-r/a)$, where σ_d^2 is the noise variance, r is the distance between two pixels, and a is the correlation length [*Fukushima et al*., 2005]. Values of $\sigma_d^2 = 5 \times 10^{-4}$ m^2 and $a = 850$ m are determined from a previous InSAR study over the volcano [*Fukushima et al*., 2010]. The residual is a linear function of the unknown offsets $\boldsymbol{o}$ inherent to the $i = 1 \ldots M$ unwrapped interferometric data and the amplitudes of the pressure ΔP and shear stress ΔS changes:

$$\boldsymbol{u_r} = \boldsymbol{u_o} - \boldsymbol{o} - \Delta P \boldsymbol{u_m^P} - \Delta S \boldsymbol{u_m^S} \tag{2}$$

where $\boldsymbol{u_m^P}$ and $\boldsymbol{u_m^S}$ are the modeled displacement for unitary pressure and shear stress changes, respectively, and

$$\boldsymbol{o} = (o_1 \boldsymbol{e}_1 \ldots o_M \boldsymbol{e_M})^T \tag{3}$$

with o_i the offset of the ith unwrapped interferometric data and $\boldsymbol{e_i} = (1 \quad \cdots \quad 1)^T$, is a vector of the same dimension as $\boldsymbol{u_o^i}$, the vector of observed displacement of the ith unwrapped interferometric data. Offsets and stress changes are determined for each forward model in order to minimize the misfit (equation (1)). The analytic solutions of $\boldsymbol{o}$, ΔP, and ΔS are given in Text S3 in the supporting information.

To decrease the computation time, the n calculations of each iteration are run simultaneously on a cluster. As a result, the computation time for an eight-parameter inversion takes only 31 h on a 60-core computer, while it requires about 40 days on a two-core computer.

The second stage of the Neighborhood Algorithm is the appraisal stage, which consists of calculating the model uncertainties following the framework of Bayesian inference [*Tarantola*, 2005]. The posterior probability density function (PPD) is estimated by resampling the population of models calculated during the first stage with a Monte Carlo integration procedure [*Sambridge*, 1999b]. Then the one-dimensional (1D-PPD) and two-dimensional (2D-PPD) marginal probability density functions are calculated and provide mean values and confidence intervals for the model parameters and indications about trade-offs between parameters, respectively.

3.2. Linear Inversion of Displacement Distribution

3.2.1. Modeling Using Meade's Method

Surface and internal displacement for strike, dip, and tensile displacement on a finite rectangular source in an elastic half-space are often computed from the analytic solutions of *Okada* [1985, 1992]. To model more complex geometries, such as nonplanar fractures, and to precisely determine displacement, *Meade*'s [2007] code for triangular dislocation elements in a uniform elastic half-space is used. Meade's code is based on *Comninou and Dundurs*'s [1975] solution for buried angular dislocation in a half-space. A triangular dislocation element is a combination of three dislocation legs, each dislocation leg being constructed by the superposition of two angular dislocations. Because the method of *Meade* [2007] is based on an elastic half-space, while the MBEM takes into account the real topography of the edifice, the geometry and location previously determined with NAMBEM is used, with the fracture translated and rotated to a depth equal to the mean depth obtained with MBEM.

3.2.2. Linear Inversion

The inversion of displacement distribution consists of minimizing the least squares cost function, subject to a smoothing constraint defined as [*Ward and Barrientos*, 1986; *Harris and Segall*, 1987; *Johnson et al*., 2001]:

$$\chi^2(m) = \|\boldsymbol{W}(\boldsymbol{u_o} - \boldsymbol{G^d m})\|^2 + \lambda^{-2}\|\boldsymbol{Lm}\|^2 \tag{4}$$

The first term of the equation is the data misfit where $\boldsymbol{u_o}$ is the observed line-of-sight displacement defined above, $\boldsymbol{G^d}$ is the matrix of Green's function which relates the modeled line-of-sight displacement to the vector of unknown displacement $\boldsymbol{m}$ in the three directions of space for each triangular element, and $\boldsymbol{W}$ is the inverse of the Cholesky decomposition of the data variance-covariance matrix, also defined above. The second term is the smoothing constraint, where $\boldsymbol{L}$ is the smoothing matrix applied to displacement distribution, such that steep gradients between neighboring dislocation elements are penalized, and λ is the regularization parameter.

For the construction of $\boldsymbol{L}$, following *Maerten et al*. [2005], the Laplacian for a triangular element is approximated using the scale-dependent umbrella operator introduced by *Desbrun et al*. [1999] for the *i*th fracture element, with adjacent elements *j* on its three sides:

$$\nabla^2 m_i = \frac{2}{H_i}\sum_{j=1}^{3}\frac{m_j - m_i}{h_{ij}} \tag{5}$$

where h_{ij} is the distance from the center of element *i* to the center of element *j*, m_j is the displacement vector of element *j*, and H_j is the sum of the element center distances. In the algorithm, only the dislocations which have three neighbors are smoothed to impose null displacement at the edges of the fracture.

The regularization parameter λ is determined using the Cross Validation Sum of Squares (CVSS) method, which measures the ability of a model to predict data omitted when fitting the model [*Wahba and Wang*, 1990]. The data are segmented into several groups. A model is calculated, omitting one part of the data. Then predicted values and the sum of squared residuals at the omitted data points are computed using this model. This operation is repeated successively for all the data groups and the total sum of squared residuals is calculated. The preferred model is the one which produces the lowest sum of squares. *Matthews and Segall* [1993] use a "leave one out" form of the CVSS, consisting of omitting data points one by one, which has the advantage of having an analytic solution. In this work, this leave one out form of the CVSS is tested, but high regularization parameters which gave an undersmoothed displacement distribution are found. We thus adopted *Augier*'s [2011] approach consisting of a four-part spatially gathered data groups.

This cost function minimization approach is equivalent to maximizing the posterior probability density function in the framework of Bayesian inference. Whether the best model $\boldsymbol{m}$ corresponds to the minimum of the misfit function or to the maximum of the posterior probability density function [*Tarantola*, 2005], it is given by

$$\boldsymbol{m} = \boldsymbol{G^{-g}u_o} \tag{6}$$

where $\boldsymbol{G^{-g}}$ is the generalized inverse defined as

$$\boldsymbol{G^{-g}} = \left(\boldsymbol{G^{d^T}C_d^{-1}G^d} + \lambda^{-2}\boldsymbol{L^TL}\right)^{-1}\left(\boldsymbol{C_d^{-1}G^d}\right)^T \tag{7}$$

The model resolution matrix $\boldsymbol{R}$ indicates how well each parameter, i.e., each fracture element displacement, is resolved given the data points' spatial distribution. The best model can be written $\boldsymbol{m} = \boldsymbol{R}\boldsymbol{m}_{\text{true}}$ where $\boldsymbol{m}_{\text{true}}$ is assumed to be the perfect model. It is defined from the generalized inverse as [*Menke*, 2012]

$$\boldsymbol{R} = \boldsymbol{G^{-g}G} \tag{8}$$

To preserve physically plausible displacement distributions, avoiding opposite displacement of nearby fracture patches, inequality constraints are imposed on the displacement components. To achieve this, the least

Table 2. Characteristics of the Six Interpolated Interferograms Used to Invert the Posteruptive Displacement

Pass	Swath	Track	Line-of-Sight Vector			Incidence Angle	Number of Subsampled Points (Total = 1803)
			East	North	Up		
Ascending	2	313	−0.347	−0.079	0.934	20.87°	300
	5	399	−0.614	−0.140	0.777	39.01°	300
	7	170	−0.657	−0.174	0.733	45.85°	304
Descending	5	048	0.578	−0.131	0.805	36.38°	297
	6	277	0.632	−0.143	0.762	40.36°	300
	7	005	0.677	−0.154	0.720	43.94°	302

squares problem with inequality constraints is transformed to a nonnegative least squares problem following the algorithm described in *Menke* [2012]. For this study, considering that the displacement of the eastern flank is mainly eastward and downward [*Peltier et al*., 2009a], and also considering that northern displacement is poorly resolved by our interferometric data, the strike slip component, which is nearly north–south, is neglected and the following inequality constraints: normal displacement is negative and dip slip is positive is imposed.

4. Data Processing

The data set used to invert the posteruptive displacement is composed of 67 ASAR interferograms, acquired along three ascending and three descending orbits (Table 2), which were selected according to their low temporal and perpendicular baselines (Table S1 in the supporting information) from a set of several hundred interferograms (for processing of interferograms, see Text S2 in the supporting information).

We focus here on a period of 14 months following the end of the eruption from May 2007 to July 2008. Time series of line-of-sight displacement are calculated following the procedure of *Lundgren et al*. [2001] for the six different tracks considered in this study. Then the displacement was temporally interpolated, assuming displacement decays exponentially, to generate six interferograms covering the exact same 14 month period from 8 May 2007 to 12 July 2008 [*Augier*, 2011].

As this study focuses on the eastern flank, the summit subsidence and the zones to the north, south, and east where there is a low coherence due to dense vegetation are masked. This results in a large deformation area (approximately 5 by 6 km^2) surrounded by a narrow band 1 or 2 km in width which is devoid of deformation. Areas affected by lava flow subsidence, areas of shadowing due to locally steep slopes, and all the pixels with a coherence of less than 0.8 are also masked. To reduce the size of the data vector, making the inversion of $\boldsymbol{C_d}$ numerically manageable while keeping relevant information, the interferograms are subsampled with a quadtree procedure [*Welstead*, 1999; *Jonsson et al*., 2002]. The subsampled data set contains 1803 points with approximately 300 points per swath (Table 2). The quadtree algorithm results in different data block sizes, with small blocks in areas of high deformation and/or steep displacement gradient and large blocks in areas of low deformation. In our case, the low deformation area is small, resulting in few subsampling points in these areas. As the low deformation areas have the same importance as high deformation areas in terms of understanding the deformation processes, the weighting of each block has to be proportional to its size. This weighting is accounted for in the variance-covariance matrix $\boldsymbol{C_d}$ of the subsampled data following the approach of *Sudhaus and Jonsson* [2009] detailed in Text S2 in the supporting information.

5. Results

In this section, results of the nonlinear and linear inversions are presented using several criteria for assessing how a model explains the data. The first criterion is the percentage of explained data (ED), estimated as

$$\mathrm{ED} = 100 - \frac{\Sigma\left(\boldsymbol{u_r^2}\right)}{\Sigma\left(\boldsymbol{u_o^2}\right)} \times 100 \tag{9}$$

where u_r and u_o are the residual and observed displacement.

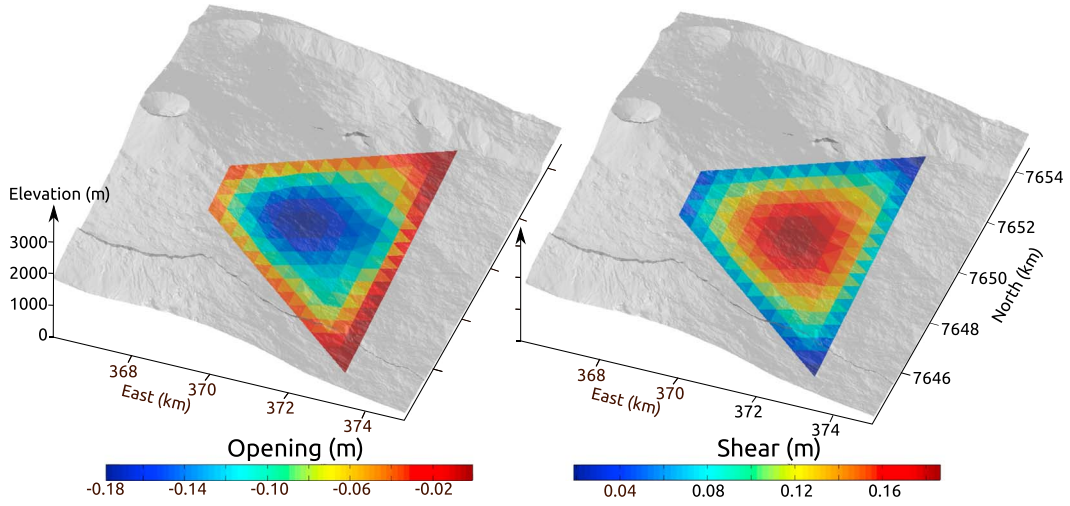

Figure 3. Normal displacement and dip slip of the simplest best fit model superimposed onto the shaded DEM. Coordinates correspond to UTM WGS84 (zone 40S).

The root-mean-square error (RMSE) is defined as

$$\mathrm{RMSE} = \sqrt{\frac{\Sigma(\boldsymbol{u}_r^2)}{p}} \tag{10}$$

with p as the number of points in the subsampled data set.

In inverse modeling, it is tempting to increase the number of parameters, adding complexity, as it improves the data fit. However, a better fit does not necessarily mean that the natural process is better reproduced and that the model is more likely. To test if increasing the number of parameters is relevant, the Akaike Information Criterion is used [*Akaike*, 1974]:

$$\mathrm{AIC} = 2k + \chi^2 + \log|\boldsymbol{C}_d| + N \times \log(2\pi) \tag{11}$$

where k is the number of inverted parameters, $|\boldsymbol{C}_d|$ is the determinant of the data variance-covariance matrix, and N is the number of data points. The more likely the model, the lower the AIC. As the same data set is used in all the inversions, the last two terms do not change and are ignored in the AIC comparison.

5.1. Nonlinear Inversion of Geometry, Location, and Homogeneous Stress Changes

5.1.1. Simplest Model

With eight parameters, fractures are planar, the stress change is homogeneous, and the rake fixed at 90°. These models correspond to null angles between the top and bottom sides of the quadrangle, and to parameters related to the circular zone of stress change cx, cy, and radius, such that they encompass the fracture. The best fit model obtained using NAMBEM is a large trapezoidal fracture (maximum width and length of 5 and 8 km, respectively) (Figure 3) with an extension similar to the deformation signal (Figure 4). The fracture is almost parallel to the topography and has sides oriented north–south (Table 3). The 2D-PPD show that there are no significant trade-offs between the model parameters (Figure S2 in the supporting information). The fracture is subject to small amplitude negative pressure and shear stress, which leads to a maximum closure of 18 cm and a maximum slip of 19 cm toward the east for the 14 month period studied (Figure 3 and Table 4). These low stress values are consistent with the large area of the fracture (25 km^2) and the small amount of posteruptive flank displacement (subsidence of ~34 cm and eastward displacement of ~15 cm over 14 months).

The RMS error on the subsampled data points is 3.2 cm which is about 10% of the observed displacement. The model reproduces 89% of the subsampled interferograms and better reproduces the ascending ones (ED = 95% compared to ED = 83% for the descending ones). The large wavelength signal in both ascending

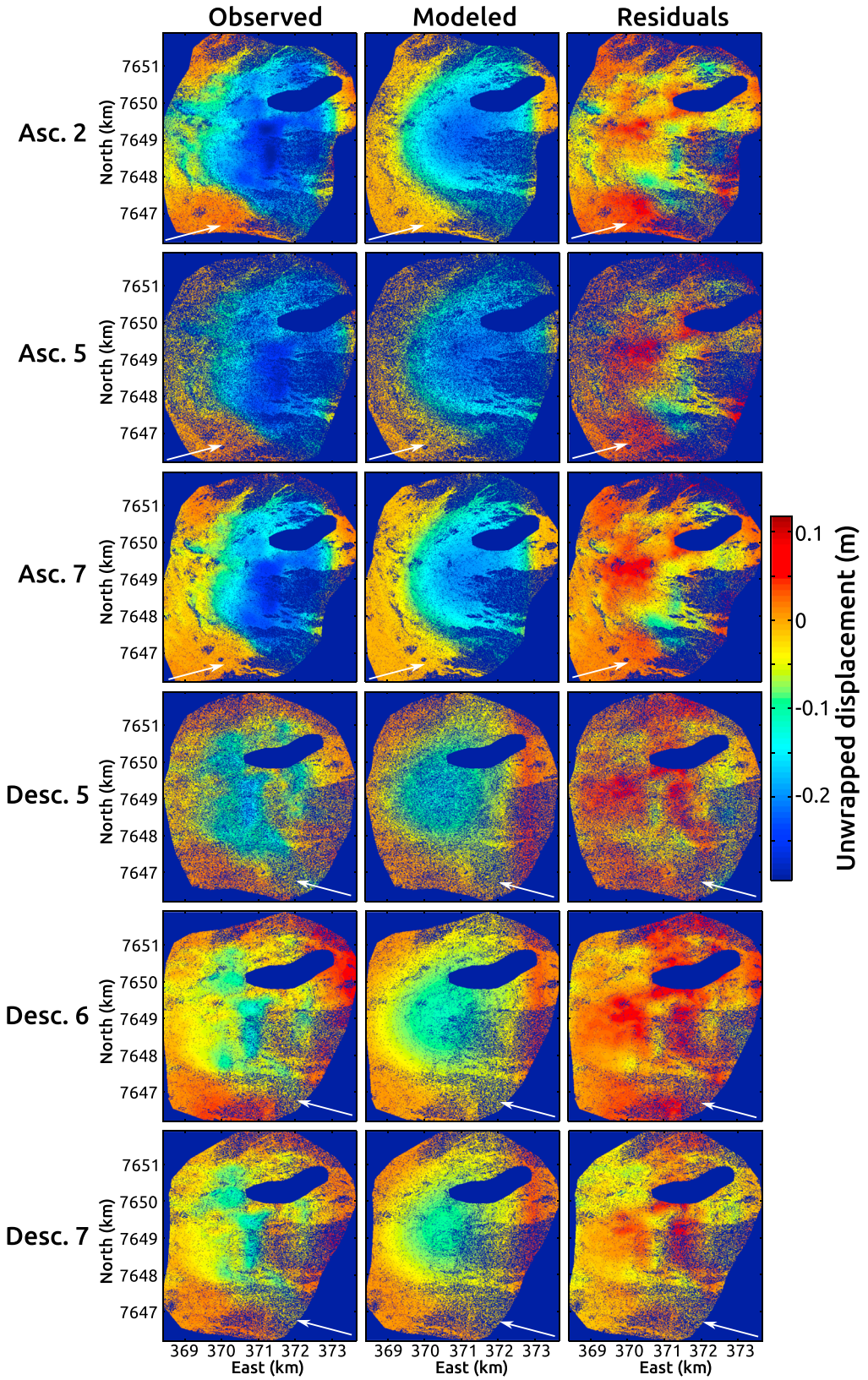

Figure 4. Observed, modeled, and residual unwrapped displacement for the simplest best fit model. Six ASAR interpolated interferograms are inverted, covering a 14 month period from May 2007 to July 2008. The white arrow represents the line-of-sight direction of the satellite. Coordinates correspond to UTM WGS84 (zone 40S).

Table 3. Best Fit Model Parameters for the Five Inversions Presented in Section 5.1.2[a]

Inversion	Simplest	Curved	Circular Patch	Distorted	Full
Number of Inverted Parameters	8	10	11	12	17
Number of Forward Models	8,648	17,863	29,425	61,158	124,431
			Best Fit Parameter and Their 95% Confidence Interval		
Midx (km) [367–372]	$368.49^{+0.1}_{-0.4}$	$369.23^{+0.5}_{-0.2}$	$368.49^{+0.6}_{-0.3}$	$368.77^{+0.2}_{-0.8}$	$368.88^{+0.01}_{-0.01}$
Midy (km) [7,646–7,652]	$7,649.03^{+0.3}_{-0.1}$	$7,649.12^{+0.3}_{-0.2}$	$7,649.03^{+0.3}_{-0.4}$	$7,648.71^{+0.2}_{-0.6}$	$7,648.9^{+0.01}_{-0.01}$
Midz (m) [−3,0007–2,500]	$1,388^{+475}_{-65}380^{+63}_{-380}$	$1,291^{+660}_{+107}776^{-121}_{-663}$	$1,328^{+746}_{+16}408^{-27}_{-408}$	$1,105^{+709}_{-8}563^{+99}_{-563}$	$788^{+5}_{-5}898^{+5}_{-45}$
mean Depth[b] (m)					
Toplen (m) [0–10,000]	$1,743^{+348}_{-319}$	$3,060^{+651}_{-931}$	$2,555^{+762}_{-1102}$	$2,325^{+1343}_{-991}$	$2,774^{+18}_{-19}$
Topang (deg) [−60–60]	*0*	*0*	*0*	-25.4^{+50}_{-33}	$-37.1^{+0.2}_{-0.3}$
Strike (deg) [−50–50]	-2^{+1}_{-2}	-1.7^{+9}_{-26}	-2.4^{+10}_{-8}	-27.4^{+54}_{-24}	$-15.2^{+0.4}_{-0.3}$
Dip (deg) [0–45]	13.7^{+2}_{-3}	11.7^{-2}_{-11}	13.4^{+3}_{-5}	22.7^{+5}_{-2}	$4.2^{+0.2}_{-0.1}$
Shear (deg) [−60–60]	*0*	*0*	*0*	-21.9^{+49}_{-28}	$-1.6^{+2}_{+0.4}$
Length (m) [1,000–10,000]	$4,745^{+554}_{-427}$	$4,411^{+718}_{-828}$	$4,698^{+936}_{-603}$	$4,722^{+186}_{-1549}$	$3,736^{+16}_{-15}$
Twist (deg) [−60–60]	*0*	*0*	*0*	20^{+35}_{+3}	$19.0^{+0.6}_{-0.5}$
Botlen (m) [500–10,000]	$8,739^{+130}_{-444}$	$7,619^{+1568}_{-971}$	$7,869^{+817}_{-1076}$	$9,299^{+505}_{-474}$	$7,466^{+19}_{-17}$
Botang (deg) [−60–60]	*0*	*0*	*0*	5.7^{+7}_{-27}	$3.2^{+0.3}_{-0.1}$
Botcurv (deg) [0–60]	*0*	31.4^{+12}_{-5}	*0*	*0*	$37.3^{+0.3}_{-0.2}$
Vertcurv (deg) [0–60]	*0*	5.5^{+10}_{-2}	*0*	*0*	$7.2^{+0.1}_{-0.1}$
Cx (km) [367–372]	*369*	*369*	$371.45^{+0.2}_{-0.7}$	*369*	$365.75^{+0.02}_{-0.05}$
Cy (km) [7,646–7,652]	*7,649*	*7,649*	$7,648.73^{+1.4}_{-1.4}$	*7,649*	$7,653.9^{+0.04}_{-0.05}$
R (m) [100–20,000]	*20,000*	*20,000*	$4,271^{+813}_{-1823}$	*20,000*	$17,431^{+28}_{-24}$
Rake (deg)	*90*	*90*	*90*	*90*	*90*

[a]The 95% confidence intervals are given as subscripts and superscripts. Search intervals are given in square brackets in the first column. Fixed parameters are in italic.
[b]The mean depth of the fracture beneath the ground surface is also given. When the mean depth equals 0, the fracture is tangential to the ground surface.

and descending lines of sight is well explained by the model (Figure 4). Some short wavelength residuals persist in the center of the pattern and at its southern and eastern sides where fringes are narrow, probably owing to the simple geometry considered here.

Because we questioned whether the obtained closure was really required to explain the surface displacement, inversions preventing fracture interpenetration were also conducted [*Cayol et al.*, 2014]. A demonstrably less good fit was obtained (RMSE = 3.52 and AIC = 2889, inversion termed "No interp" in Table 4), which indicates that closure of the fracture is the most likely model.

5.1.2. Making the Source Geometry More Complex

In this section, we investigate whether a more complex geometry can improve the data fit. Inversions of progressively increasing model complexity are performed, the rake still being fixed at 90°, with the Akaike Information Criterion, defined in equation (11) being used to evaluate the data fit improvement. An inversion termed "curved" allows the fracture to be curved (10 parameters, adding botcurv and vertcurv, Table 1). Another termed "circular patch" considers that stress changes take place on a circular patch (11 parameters,

Table 4. Stress Amplitudes and Displacement on the Fracture and Model Evaluation Criteria for the Five Inversions Presented in Section 5.1.2, the Inversion Preventing Fracture Interpenetration, and the Linear Inversion of Displacement Distribution

Inversion	Simplest	Curved	Circular Patch	Distorted	Full	No Interp	Linear
			Stresses and Displacement on the Fracture				
Pressure (MPa)	−0.014	−0.045	−0.015	0.0027	−0.068	0	not inverted
Shear Stress Drop (MPa)	0.073	0.15	0.073	0.13	0.16	0.41	not inverted
Mean/Max. Opening (cm)	−8.7/−18	−7.8/−15	−9.1/−18	−7/−16	−9.7/−20	0.3/1.2	−4.6/−22
Mean/Max. Slip (cm)	11/19	17/26	11/18	15/25	22/42	47/66	4.8/17
			Model Evaluation				
RMSE (cm)	3.22	3.37	3.12	3.21	3.00	3.52	2.30
AIC	2795	2776	2806	2694	2599	2889	4436

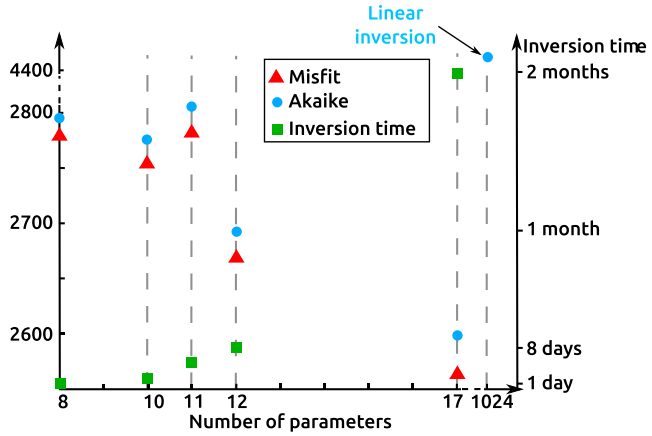

Figure 5. Misfit and Akaike Information Criteria and duration of each inversion as a function of the number of inverted parameters. Note that the left and bottom axes have been cut to allow the representation of the linear inversion of displacement distribution (for this point, the inversion time is a few minutes).

adding cx, cy, and radius). An inversion termed "distorted" distorts the quadrangle, introducing inclinations between the bottom and the top lines of the quadrangle (12 parameters, adding topang, botang, shear, and twist). Finally, all the defined parameters are simultaneously inverted in the inversion termed "full" (17 parameters).

Figure 5 and Table 4 show that when the number of parameters is increased, the AIC decreases and the model becomes more likely, indicating that the fracture complexities introduced are relevant. The circular patch model is the exception as it has a larger AIC. Indeed, the inverted circular patch is larger than the fracture, corresponding to homogeneous stress changes over the whole fracture, so the three parameters cx, cy, and radius do not provide any information. However, these parameters could improve the AIC in other volcanic or tectonic contexts. The total inversion time is an exponential function of the number of parameters, according to the number of models in the first step of the inversion (section 3.1.2).

All the inversions converge toward a trapezoidal fracture with a low dip to the east (dip of 4 to 23°) and with width and length of 5 and 8 km (Figure 6 and Table 3). Inverting for curvatures leads to a significant along-strike (botcurv = 30–37°) and a low along-dip (vertcurv = 5–7°) curvature. Allowing for a distorted quadrangle

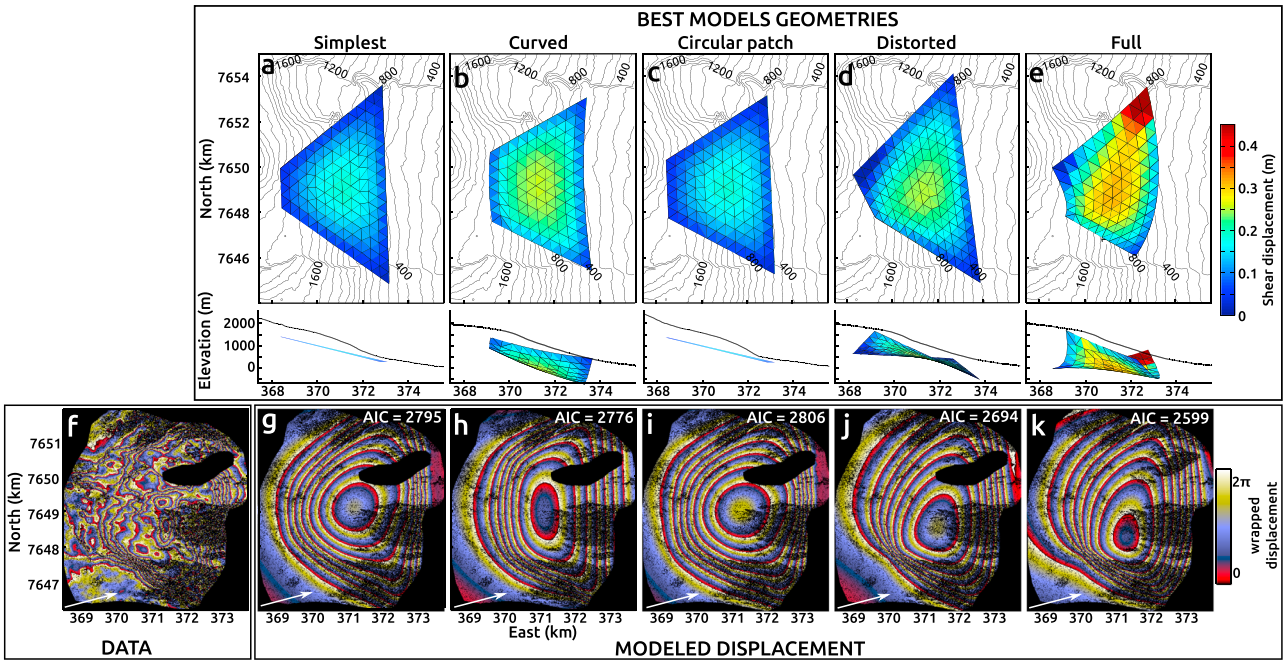

Figure 6. (top) Best fit model geometries and (bottom) wrapped displacement projected in ascending swath 2 for (a, g) the simplest model inversion (8 parameters), (b, h) inversion with curvatures ("curved," 10 parameters), (c, i) inversion with a circular stress change patch ("circular patch," 11 parameters), (d, j) inversion with angles between the bottom line and the top line of the quadrangle ("distorted," 12 parameters), (e, k) inversion including all these parameters ("full," 17 parameters). (f) Observed displacement in ascending swath 2 from May 2007 to July 2008. The Akaike criteria (AIC) is shown in white. The area of these plots is marked on Figures 1b–1e. Coordinates correspond to UTM WGS84 (zone 40S).

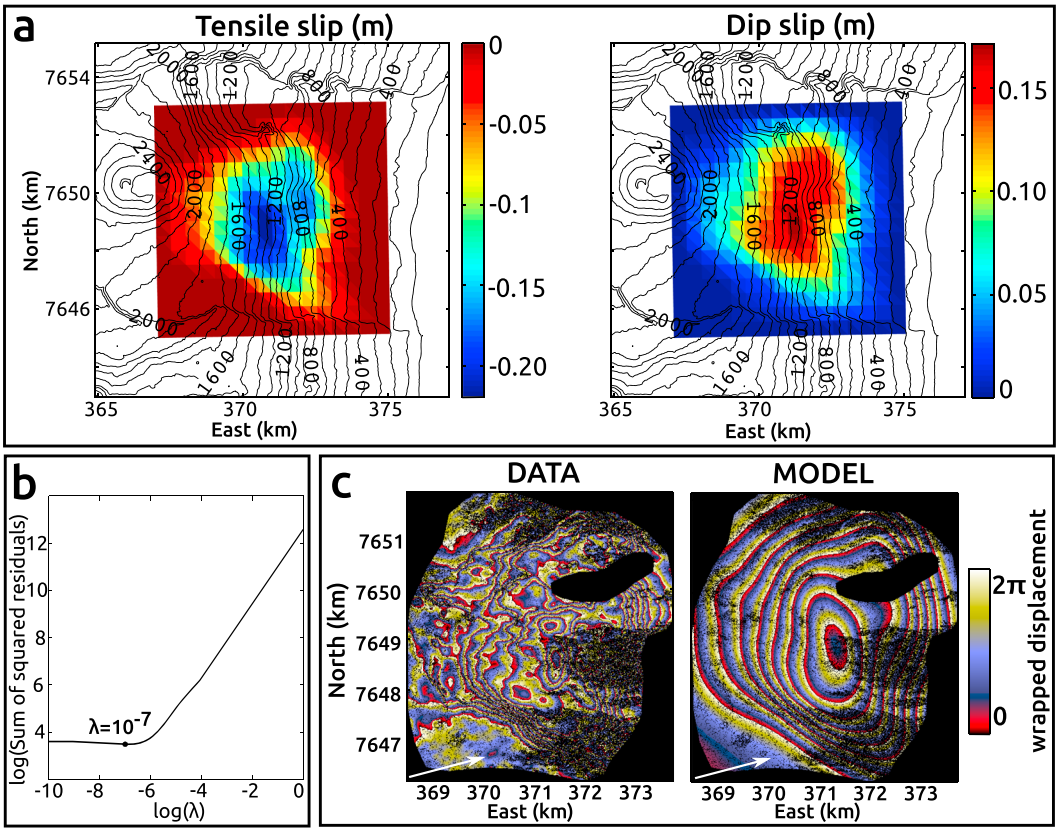

Figure 7. Best displacement distribution model with an elastic half-space. (a) Normal displacement and dip slip. Positive normal displacement corresponds to opening and positive dip slip indicates eastward displacement. (b) Sum of squared residuals determined by CVSS for λ from 0 to 10^{-10}. The minimum is used to compute the displacement distribution. (c) Observed and modeled displacement projected in ascending swath 2, covering a period from May 2007 to July 2008. Coordinates correspond to UTM WGS84 (zone 40S).

by inverting for angles between bottom and top lines leads to a quadrangle with a southwest corner near the ground surface. This geometry improves the data fit, which is particularly visible in the southern part of the eastern flank where fringes are narrow. Though we demonstrate that increasing the number of parameters allows to better explain the subsampled data, geometries of the inverted model are not markedly different enough, so we mainly discuss the simplest model in the rest of this paper.

5.2. Linear Inversion of Displacement Distribution

The simplest model geometry found with NAMBEM is used to invert the displacement distribution using the half-space solution of *Meade* [2007]. The fracture geometry and the displacement distribution could have simultaneously been inverted using this method. However, a previous study [*Fukushima et al*., 2005] showed that neglecting topography leads to a bias in the estimated geometry and locations. To compensate for the flat topography and have a geometry following the topography, as determined by the previous inversion, the fracture is translated and rotated to a depth equal to the mean depth obtained with NAMBEM (−380 m). The fracture is also extended to form an 8 by 8 km square, making it larger than the trapezoidal fracture previously determined so that the results are more general. The fracture is discretized into 512 triangular elements, and as the normal displacement and the dip slip are resolved, the number of unknowns is 1024. This is less than the number of subsampled data points (1803 points), so the numerical problem is overdetermined. Hence, the displacement distribution is well resolved, as is shown with the resolution matrix (equation (8)) equal to 1. The smoothing parameter obtained with CVSS is $\lambda = 10^{-7}$ (Figure 7b). The results of this inversion termed "linear" are summarized in Table 4. The RMS error calculated on the subsampled data points is 2.3 cm, and the model is able to explain 93% of the subsampled interferograms, with the ascending

interferograms (ED of 97%) being better explained than the descending ones (ED of 89%), as for the nonlinear inversion.

6. Discussion

6.1. Comparison Between Nonlinear and Linear Inversions

The displacement distribution obtained with the linear inversion, given the fracture, has a trapezoidal pattern, consistent with the trapezoidal shape obtained with the nonlinear inversion of the source geometry (Figure 7a). In the same way as for the nonlinear inversion, closure and eastward displacement are obtained. As expected, the displacement distributions is less smooth than for the linear inversion with homogeneous stresses. However, the maximum amplitudes of normal displacement and dip slip on the fracture are also similar, with up to -22 cm and 17 cm, respectively. Given the similar displacement distributions obtained with nonlinear and linear inversions, we conclude that stress homogeneity hypothesis of the MBEM is acceptable for this study. The linear inversion leads to a better fit for the data, but because of the large number of model parameters, the AIC (4436) is higher, indicating that this model is less likely than the nonlinear inversion (Figure 5). For both methods, the descending data are less well explained than the ascending data, indicating that the model geometry might be responsible for the inability of the model to fully explain the data.

6.2. Origin of Flank Displacement

The inversions of the April 2007 posteruptive displacement with nonlinear and linear inversions give similar results: a shallow, large area trapezoidal fracture subparallel to the topography is able to reproduce most of the displacement. Contrary to the cases of Kilauea, Etna, and Cumbre Vieja volcanoes, where deep low-angle faults have been identified (8 km deep décollement, 1 to 3 km deep detachment, and 2 to 4 km deep detachment, respectively), the obtained fracture is very shallow beneath the eastern flank of Piton de la Fournaise (mean depth of 380 m). The depth is closer to that of the fracture identified at Stromboli, but the dip angle is lower. In a similar way to these different studies, the fracture is probably following a preexisting lithological discontinuity, as indicated by the ground-parallel geometry we find. Such lithological discontinuities have been evidenced by an exploration drilling east of this fracture [*Rançon et al*., 1989]. However, unlike these studies in which faults were identified, closure of the fracture with simultaneous slip is obtained. Small amplitude negative pressure (-0.014 MPa/yr) and shear stress (0.073 MPa/yr) are determined, which is mechanically consistent with the small amount of displacement in the posteruptive period (subsidence of ~34 cm and eastward displacement of ~15 cm) and the large surface area of the fracture (25 km^2). If displacement was due to gravity alone acting on a discontinuity, amplitudes of the pressure and shear stress changes would be proportional to the normal and tangential projection of the gravitational force on the fracture, respectively. Therefore, the ratio between shear stress and pressure would be $\Delta\tau/\Delta P \approx \tan(\mathrm{dip}) \approx 0.18 - 0.27$ (considering the 95% confidence intervals of the dip, which is 10° to 15°). Here the shear stress is greater than the pressure change, leading to $\Delta\tau/\Delta P = 5.2$, which indicates that gravity is not the main force and that an additional shear force drives the motion of the eastern flank toward the east. As determined for Kilauea [*Dieterich*, 1988; *Dieterich et al*., 2000; *Iverson*, 2005; *Denlinger and Morgan*, 2014; *Montgomery-Brown et al*., 2015] and Etna [*Lundgren et al*., 2003; *Apuani et al*., 2013; *Bonaccorso et al*., 2013], repeated dyke intrusions build up stresses, and progressively drive the flank to failure. When critical equilibrium is reached, any suitably oriented intrusive events can trigger flank destabilization. For Piton de la Fournaise, this process could play a major role in flank destabilization. Indeed, before the March–April 2007 crises, the activity of Piton de la Fournaise has been intense with 25 summit eruptions since 1981 [*Peltier et al*., 2009a]. *Michon et al*. [2009] estimated that 68% of these eruptions occurred in the N25°–30° rift zones, indicating that this axis is the preferred intrusion axis for the volcano. These repeated intrusions bring the eastern flank close to failure. The 30 March intrusion or a sill intrusion could have triggered the April 2007 flank displacement event, as indicated by the timing of the displacement observed at cGPS summit stations [*Got et al*., 2013].

The negative pressure is not surprising as it is the posteruptive displacement, when lava eruption has resumed, that is being studied. The closure takes place after the end of the eruption and might be related to the coeruptive uplift observed during the eruption (Figure 1c). Following the hypothesis of a sheared sill, we investigate whether the closure could be related to a sill emplaced under the eastern flank, which could have fed the eruptive fissure during the April 2007 eruption, as suggested by *Got et al*. [2013], *Chaput et al*.

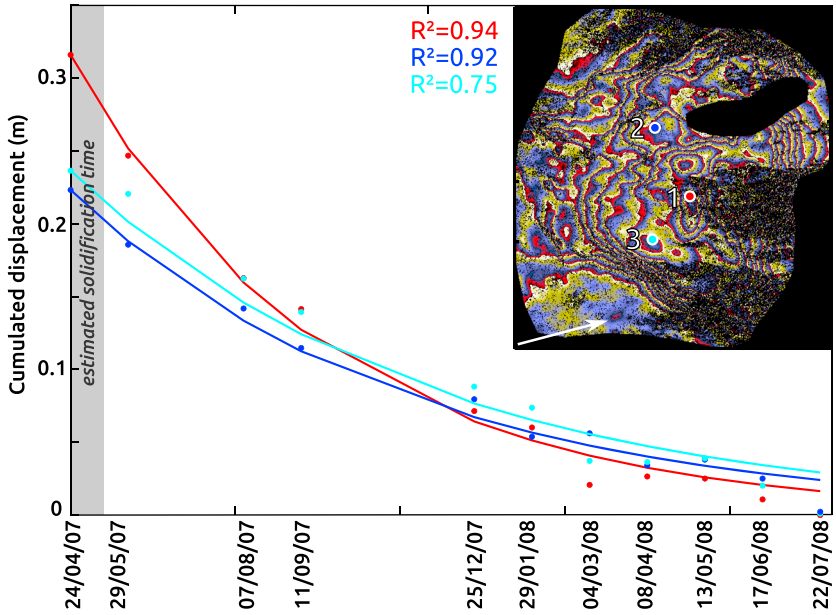

Figure 8. Posteruptive displacement versus time computed from time series (points) and their best fitting exponential curves for three pixels of an ascending interferogram (swath 2) located in the eastern flank. The subplot gives the location of the three pixels. Pixel 1 is located at the point of maximum posteruptive displacement rate. Pixels 2 and 3 are good indicators of the mean displacement rate of the whole flank. Correlation coefficients of the exponential curves R^2 are shown.

[2014a], and *Froger et al*. [2015]. In this scenario, the posteruptive closure could be due either to thermal contraction and/or degassing of magma contained in the sill.

6.2.1. Thermal Contraction and Degassing

The extreme case, where the maximum value of the closure (18 cm) recorded during the 14 month posteruptive period is due to thermal contraction, is considered, since sills contract as they cool by conduction of excess heat to the adjacent country rock. The initial thickness required to obtain thermal contraction of 18 cm is estimated. From a one-dimensional approximation, this thickness would be $h_0 = \Delta h/(\alpha \Delta T)$ [*Turcotte and Schubert*, 2002], where Δh is the amount of contraction due to cooling, $\alpha = 5 \times 10^{-5} K^{-1}$ [*Huppert and Sparks*, 1988] is the coefficient of thermal expansion of the basaltic magma, $\Delta T = T - T_0$ is the temperature change of the cooling sill, with $T = 35℃$ the temperature of the host rock at the sill depth (~380 m) and $T_0 = 1150℃$ the temperature of magma emplaced in the sill. These values give an initial thickness of 3.2 m. A computation shows that the intrusion of a sill of such a thickness at the estimated depth would create an uplift of the order of 3 m, yet the maximum inflation observed in the eastern flank during the coeruptive period amounts to only 35 cm [*Froger et al*., 2015].

In addition, the solidification time of a 3.2 m thick sill is estimated from a one-dimensional solution as follows: $t_s = \frac{b^2}{4\kappa\lambda_2^2}$ [*Turcotte and Schubert*, 2002], where b is the intrusion half width and $\kappa = 7.4 \times 10^{-7} m^2\ s^{-1}$ [*Bernabeu*, 2012] is the thermal diffusivity. The coefficient $\lambda_2 = 0.7$ is estimated [from *Turcotte and Schubert*, 2002, Figure 4.36] from the latent heat $L = 4 \times 10^5\ J\ kg^{-1}$ and the specific heat $c = 1225\ J\ kg^{-1}\ K^{-1}$ [*Bernabeu*, 2012], and the temperature difference between the magma and the host rock ΔT. $t_s = 20$ days is calculated. For comparison, flank displacement rates are computed by time series interpolation at three interferogram pixels representative of the maximum and mean flank displacements (Figure 8). Fitting these displacements using a decreasing exponential of the form $d = ae^{-t/\tau} + b$ with τ, relaxation times of 154, 204, and 217 days for pixels 1, 2, and 3, respectively, the total subsidence duration is estimated by extrapolating these curves, assuming that the deformation ends when the displacement is 1% of its initial value. Overall subsidence durations of 24, 31, and 33 months for pixels 1 to 3 are determined. The estimated solidification time represents only 2% of the estimated subsidence time. Both the thickness and the solidification time of the presumed sill are incompatible with our observations; hence, we conclude that the eastern flank deformation cannot be explained by the thermal contraction of a sill.

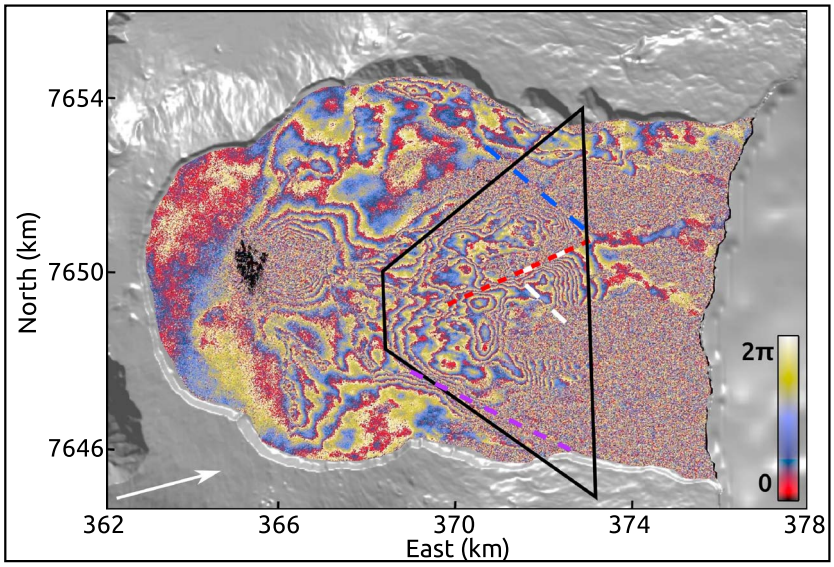

Figure 9. Possible structural influence affecting the posteruptive deformation of the eastern flank. The ascending interferogram of swath 2 is overlain onto the DEM. The black line is the trace of the simplest best fit quadrangle. The red dotted line is the N65° fault [*Michon and Saint-Ange*, 2008]. The purple and blue dotted lines are the N120° and the N130°–140° buried discontinuities, respectively, that seem to control the extent of the deformation. The white dotted line represents the "V-shaped" structure. Coordinates correspond to UTM WGS84 (zone 40S).

Degassing of magma contained in the sill can also lead to contraction. However, this process only occurs during cooling of the sill when the magma is still fluid. Considering the inferred solidification time, contraction due to degassing could only have occurred during the 20 days after the sill emplacement, which is not consistent with the observed duration of the subsidence. Therefore, a degassing of a sill cannot explain the eastern flank deformation either.

As alternatives, the posteruptive eastern flank displacement could be induced by the ongoing slip and poroelastic and viscoelastic compaction above a coeruptive detachment fracture or simply the closure of a coeruptive detachment fracture previously folded as it was sheared [*Homza and Wallace*, 1995]. Study of the coeruptive deformation and associated processes are beyond the scope of this paper, but they will be investigated in another study.

6.2.2. A Structural Influence?

Inverting for more complex geometries (section 5.1.2), we showed that a quadrangular fracture whose southwest side becomes vertical and reaches close to the ground surface better reproduces the narrow fringes to the south of the deformation signal. From this result, we postulate that a ~N120° discontinuity at the south of the Grandes Pentes might have been active during the posteruptive period (Figure 9). This fault might be buried as it is not visible in the topography.

Moreover, a N65° trending normal fault linking the southern side of the summit cone to a "V-shaped" structure [*Bachèlery*, 1981] in the northern part of the Grandes Pentes has been proposed by *Michon and Saint-Ange* [2008]. All posteruptive interferograms show about two fringes of deformation almost perfectly aligned with this structure (Figure 9). We therefore propose that the N65° fault was active during the posteruptive period. North of the "V-shaped" structure, a N130°–140° discontinuity corresponding to a strong slope change may also have played a role in the structural control by limiting the northern extent of the displacement.

Inversions taking into consideration the main quadrangle and several faults could improve our understanding of the structural control involved during the posteruptive period. However, such inversions are very challenging as they require a very high number of nonlinear parameters and would only lead to a marginal improvement of the data fit, as 89% of the data are already explained by our best fit model.

7. Conclusions

In this paper, following the observation of sheared sills at Piton des Neiges volcano [*Famin and Michon*, 2010], we present a new method for inverting displacement assuming the source is submitted to both pressure and shear stress changes. The method is based on nonlinear inversions combining a Mixed Boundary Element modeling method [*Cayol and Cornet*, 1997] with a Neighborhood Algorithm [*Sambridge*, 1999a; *Fukushima et al*., 2005]. Stress changes are assumed to take place over a circular patch of a curved quadrangular source.

We apply this method to the large seaward displacement of the eastern flank observed by InSAR after the April 2007 eruption of Piton de la Fournaise. The data set is composed of Envisat interferograms from six different lines of sight which have been temporally interpolated to cover the same period. Data are subsampled with a quadtree algorithm and a full covariance matrix is taken into account, such that it gives equal weight to deformed and nondeformed areas.

We determine that a very shallow (mean depth of 380 m) 5 by 8 km trapezoidal fracture subparallel to the ground, probably coincident with a lithological discontinuity such as those identified by an exploration drilling east of this fracture, is able to reproduce 90% of the observed deformation. Small amplitude pressure and shear stress changes, corresponding to closure and seaward slip of a fracture, are determined. Respective amounts of pressure and shear stress changes indicate that the driving force for the posteruptive flank displacement is not only due to gravity but that shear forces, which probably accumulated during previous dyke intrusions, are relaxed. A more complex geometry, corresponding to a curved fracture whose southwestern corner approaches the surface, enables the Akaike information criterion to be improved corresponding to a more likely model. Linear inversion of displacement distribution in a half-space, given the previously determined fracture geometry, gives similar normal displacement and slip but does not lead to a more likely solution. Therefore, we conclude that the stress homogeneity hypothesis of the NAMBEM is valid in our case and that unexplained displacement is probably due to a more complex source geometry. Based on the observation of fringe patterns on interferograms, we postulate that the eastern flank deformation has been influenced by several faults. The N65° normal fault identified by *Michon and Saint-Ange* [2008] and a N120° discontinuity to the south of the Grandes Pentes were probably active during the posteruptive period.

The negative pressure obtained for the posteruptive period could be explained by thermal contraction or degassing of magma, following the hypothesis of the emplacement of a sheared sill during the April 2007 eruption. However, the solidification time determined for this shallow sill is short (~20 days) compared to the duration of the subsidence, estimated at 24 to 33 months. Consequently, thermal contraction or degassing of a sill cannot explain the posteruptive deformation of the eastern flank. The posteruptive eastern flank displacement could alternatively result from the compaction and the ongoing slow slip on a shallow detachment fault.

Future work will focus on the coeruptive geodetic data to investigate the source of the large 1.4 m seaward displacement. We believe that it could improve understanding of the mechanism which caused the closure of the fracture during the posteruptive period. As there are widespread field observations of coeval normal and shear displacement, such joint inversions should be undertaken more often when interpreting geodetic data.

Acknowledgments

The authors would like to especially thank Fran Van Wyk de Vries for proofreading this manuscript. The PhD fellowship of Marine Tridon is founded by the french Ministère de l'Education Nationale, de l'Enseignement Supérieur et de la Recherche. This research was supported by INSU-CNRS grants of the Aléas program. We thank the European Space Agency for providing the ASAR data through the AO-Envisat project 746. The ASAR interferograms were produced with the Diapason Software. All the interferograms used in this study are available on the CASOAR web interface created by the Service d'Observation OI^2 of the Observatoire de Physique du Globe de Clermont-Ferrand by following this link: https://wwwobs.univ-bpclermont.fr/casoar/index_liste.php. We thank P. Gouinaud and collaborators for giving us the opportunity to use the cluster of ISIMA to launch the inversions. We also thank V. Famin, L. Michon, T. Menand, and A. Di Muro for useful discussions about this study. Comments made by two anonymous reviewers help us to improve the manuscript. This is Laboratory of Excellence ClerVolc contribution 217.

References

Akaike, H. (1974), A new look at the statistical model identification, *IEEE Trans. Autom. Control*, *19*(6), 716–723, doi:10.1109/TAC.1974.1100705.

Amelung, F., S. Jonsson, H. Zebker, and P. Segall (2000), Widespread uplift and "trapdoor" faulting on Galapagos Volcanoes observed with radar interferometry, *Nature*, *407*, 993–996, doi:10.1038/nature01526.1.

Ando, M. (1979), The Hawaii earthquake on November 29, 1975: Low dip angle faulting due to forceful injection of magma, *J. Geophys. Res.*, *84*(B13), 7616–7626, doi:10.1029/JB084iB13p07616.

Apuani, T., C. Corazzato, A. Merri, and A. Tibaldi (2013), Understanding Etna flank instability through numerical models, *J. Volcanol. Geotherm. Res.*, *251*, 112–126, doi:10.1016/j.jvolgeores.2012.06.015.

Arnadottir, T., and P. Segall (1991), A fault model for the 1989 Kilauea south flank earthquake from leveling and seismic data, *Geophys. Res. Lett.*, *18*(12), 2217–2220, doi:10.1029/91GL02691.

Augier, A. (2011), Étude de l'éruption d'avril 2007 du Piton de la Fournaise (île de La Réunion) à partir de données d'interférométrie RADAR et GPS, développement et application de procédures de modélisation, PhD thesis, Université Blaise Pascal, Clermont-Ferrand.

Bachélery, P. (1981), *Le Piton de la Fournaise (Ile de la Réunion): Etude volcanologique, structurale et pétrologique*, PhD thesis, Université Blaise Pascal, Clermont-Ferrand.

Baldi, P., M. Coltelli, M. Fabris, M. Marsella, and P. Tommasi (2008), High precision photogrammetry for monitoring the evolution of the NW flank of Stromboli Volcano during and after the 2002–2003 eruption, *Bull. Volcanol.*, *70*(6), 703–715, doi:10.1007/s00445-007-0162-1.

Beauducel, F., and D. Carbone (2015), A strategy to explore the topography-driven distortions in the tilt field induced by a spherical pressure source: The case of Mt Etna, *Geophys. J. Int.*, *201*(3), 1471–1481, doi:10.1093/gji/ggv076.

Beauducel, F., and F. H. Cornet (1999), Collection and three-dimensional modeling of GPS and tilt data at Merapi volcano, Java, *J. Geophys. Res.*, *104*(B1), 725–736, doi:10.1029/1998JB900031.

Bernabeu, N. (2012), *Modélisation des coulées volcaniques, master thesis*, Université de la Réunion.

Berthod, C., V. Famin, J. Bascou, L. Michon, B. Ildefonse, and P. Monié (2016), Evidence of sheared sills related to flank destabilization in a basaltic volcano, *Tectonophysics*, *674*, 195–209, doi:10.1016/j.tecto.2016.02.017.

Boivin, P., and P. Bachèlery (2009), Petrology of 1977 to 1998 eruptions of Piton de la Fournaise, La Réunion Island, *J. Volcanol. Geotherm. Res.*, *184*(1–2), 109–125, doi:10.1016/j.jvolgeores.2009.01.012.

Bonaccorso, A., G. Currenti, and C. Del Negro (2013), Interaction of volcano-tectonic fault with magma storage, intrusion and flank instability: A thirty years study at Mt. Etna Volcano, *J. Volcanol. Geotherm. Res.*, *251*, 127–136, doi:10.1016/j.jvolgeores.2012.06.002.

Bonforte, A., and G. Puglisi (2003), Magma uprising and flank dynamics on Mount Etna Volcano, studied using GPS data (1994–1995), *J. Geophys. Res.*, *108*(B3), 2153, doi:10.1029/2002JB001845.

Cayol, V., and F. H. Cornet (1997), 3D mixed boundary elements for elastostatic deformation field analysis, *Int. J. Rock Mech. Min. Sci.*, *34*(2), 275–287, doi:10.1016/S0148-9062(96)00035-6.

Cayol, V., and H. Cornet (1998), Effects of topography on the interpretation of the deformation field of prominent volcanoes—Application to Etna, *Geophys. Res. Lett.*, *25*(11), 1979–1982, doi:10.1029/98GL51512.

Cayol, V., J. H. Dieterich, A. T. Okamura, and A. Miklius (2000), High magma storage rates before the 1983 eruption of Kilauea, Hawaii, *Science*, *288*(5475), 2343–2346, doi:10.1126/science.288.5475.2343.

Cayol, V., T. Catry, L. Michon, M. Chaput, V. Famin, O. Bodart, J.-L. Froger, and C. Romagnoli (2014), Sheared sheet intrusions as mechanism for lateral flank displacement on basaltic volcanoes: Applications to Réunion Island volcanoes, *J. Geophys. Res. Solid Earth*, *119*, 7607–7635, doi:10.1002/2014JB011139.

Chaput, M., V. Pinel, V. Famin, L. Michon, and J.-L. Froger (2014a), Cointrusive shear displacement by sill intrusion in a detachment: A numerical approach, *Geophys. Res. Lett.*, *41*, 1937–1943, doi:10.1002/2014GL061184.

Chaput, M., V. Famin, and L. Michon (2014b), Deformation of basaltic shield volcanoes under cointrusive stress permutations, *J. Geophys. Res. Solid Earth*, *119*, 5814–5829, doi:10.1002/2014JB011151.

Cianetti, S., C. Giunchi, and E. Casarotti (2012), Volcanic deformation and flank instability due to magmatic sources and frictional rheology: The case of Mount Etna, *Geophys. J. Int.*, *191*(3), 939–953, doi:10.1111/j.1365-246X.2012.05689.x.

Comninou, M., and J. Dundurs (1975), The angular dislocation in a half space, *J. Elast.*, *5*(3–4), 203–216, doi:10.1007/BF00126985.

Delaney, P. T. (1986), Emplacement processes and paleostress analysis, *J. Geophys. Res.*, *91*(B5), 4920–4938, doi:10.1029/JB091iB05p04920.

Delaney, P. T., R. S. Fiske, A. Miklius, A. T. Okamura, and M. K. Sako (1990), Deep magma body beneath the summit and rift zones of Kilauea Volcano, Hawaii, *Science*, *247*, 3–8.

Denlinger, R. P., and J. K. Morgan (2014), Instability of Hawaiian volcanoes, in *Characteristics of Hawaiian Volcanoes*, *U.S. Geol. Surv. Prof. Pap.*, 1801, pp. 149–176.

Desbrun, M., M. Meyer, P. Schröder, and A. H. Barr (1999), Implicit fairing of irregular meshes using diffusion and curvature flow, *Proc. 26th Annu. Conf. Comput. Graph. Interact. Tech.—SIGGRAPH '99*, *33*, 317–324, doi:10.1145/311535.311576.

Desmarais, E. K., and P. Segall (2007), Transient deformation following the 30 January 1997 dike intrusion at Kilauea Volcano, Hawai'i, *Bull. Volcanol.*, *69*(4), 353–363, doi:10.1007/s00445-006-0080-7.

Di Muro, A., N. Métrich, D. Vergani, M. Rosi, P. Armienti, T. Fougeroux, E. Deloule, I. Arienzo, and L. Civetta (2014), The shallow plumbing system of Piton de la Fournaise Volcano (La Réunion Island, Indian Ocean) revealed by the major 2007 caldera-forming eruption, *J. Petrol.*, *55*(7), 1287–1315, doi:10.1093/petrology/egu025.

Di Traglia, F., T. Nolesini, E. Intrieri, F. Mugnai, D. Leva, M. Rosi, and N. Casagli (2014), Review of ten years of volcano deformations recorded by the ground-based InSAR monitoring system at Stromboli Volcano: A tool to mitigate volcano flank dynamics and intense volcanic activity, *Earth Sci. Rev.*, *139*, 317–335, doi:10.1016/j.earscirev.2014.09.011.

Dieterich, J. (1988), Growth and persistence of Hawaiian volcanic rift zones, *J. Geophys. Res.*, *93*(B5), 4258–4270, doi:10.1029/JB093iB05p04258.

Dieterich, J. H., V. Cayol, and P. G. Okubo (2000), The use of earthquake rate changes as a stress meter at Kilauea volcano, *Nature*, *408*, 457–460, doi:10.1038/35044054.

Famin, V., and L. Michon (2010), Volcano destabilization by magma injections in a detachment, *Geology*, *38*, 219–222, doi:10.1130/G30717.1.

Famin, V., B. Welsch, S. Okumura, P. Bachèlery, and S. Nakashima (2009), Three differentiation stages of a single magma at Piton de la Fournaise volcano (Reunion hot spot), *Geochem. Geophys. Geosyst.*, *10*, Q01007, doi:10.1029/2008GC002015.

Froger, J.-L., Y. Fukushima, P. Briole, T. Staudacher, T. Souriot, and N. Villeneuve (2004), The deformation field of the August 2003 eruption at Piton de la Fournaise, Reunion Island, mapped by ASAR interferometry, *Geophys. Res. Lett.*, *31*, L14601, doi:10.1029/2004GL020479.

Froger, J.-L., V. Famin, V. Cayol, A. Augier, L. Michon, and J.-F. Lénat (2015), Time-dependent displacements during and after the April 2007 eruption of Piton de la Fournaise, revealed by interferometric data, *J. Volcanol. Geotherm. Res.*, *296*, 55–68, doi:10.1016/j.jvolgeores.2015.02.014.

Fukushima, Y., V. Cayol, and P. Durand (2005), Finding realistic dike models from interferometric synthetic aperture radar data: The February 2000 eruption at Piton de la Fournaise, *J. Geophys. Res.*, *110*, B03206, doi:10.1029/2004JB003268.

Fukushima, Y., V. Cayol, P. Durand, and D. Massonnet (2010), Evolution of magma conduits during the 1998–2000 eruptions of Piton de la Fournaise Volcano, Réunion Island, *J. Geophys. Res.*, *115*, B10204, doi:10.1029/2009JB007023.

Fukushima, Y., Y. Takada, and M. Hashimoto (2013), Complex ruptures of the 11 April 2011 *Mw* 6.6 Iwaki earthquake triggered by the 11 March 2011 *Mw* 9.0 Tohoku earthquake, Japan, *Bull. Seismol. Soc. Am.*, *103*(2), 1572–1583, doi:10.1785/0120120140.

Gonzalez, P. J., K. F. Tiampo, A. G. Camacho, and J. Fernandez (2010), Shallow flank deformation at Cumbre Vieja Volcano (Canary Islands): Implications on the stability of steep-sided volcano flanks at oceanic islands, *Earth Planet. Sci. Lett.*, *297*(3–4), 545–557, doi:10.1016/j.epsl.2010.07.006.

Got, J. L., A. Peltier, T. Staudacher, P. Kowalski, and P. Boissier (2013), Edifice strength and magma transfer modulation at Piton de la Fournaise Volcano, *J. Geophys. Res. Solid Earth*, *118*, 5040–5057, doi:10.1002/jgrb.50350.

Grosfils, E. B. (2007), Magma reservoir failure on the terrestrial planets: Assessing the importance of gravitational loading in simple elastic models, *J. Volcanol. Geotherm. Res.*, *166*(2), 47–75, doi:10.1016/j.jvolgeores.2007.06.007.

Harris, R. A., and P. Segall (1987), Detection of a locked zone at depth on the Parkfield, California, segment of the San Andreas Fault, *J. Geophys. Res.*, *92*(B8), 7945–7962, doi:10.1029/JB092iB08p07945.

Homza, T. X., and W. K. Wallace (1995), Geometric and kinematic models for detachment folds with fixed and variable detachment depths, *J. Struct. Geol.*, *17*(4), 575–588, doi:10.1016/0191-8141(94)00077-D.

Hooper, A., B. Ófeigsson, F. Sigmundsson, B. Lund, P. Einarsson, H. Geirsson, and E. Sturkell (2011), Increased capture of magma in the crust promoted by ice-cap retreat in Iceland, *Nat. Geosci.*, *4*(11), 783–786, doi:10.1038/ngeo1269.

Huppert, H. E., and R. S. J. Sparks (1988), The fluid dynamics of crustal melting by injection of basaltic sills, *Trans. R. Soc. Edinb. Earth Sci.*, *79*(2–3), 237–243, doi:10.1017/S0263593300014243.

Intrieri, E., F. Di Traglia, C. Del Ventisette, G. Gigli, F. Mugnai, G. Luzi, and N. Casagli (2013), Flank instability of Stromboli volcano (Aeolian Islands, Southern Italy): Integration of GB-InSAR and geomorphological observations, *Geomorphology*, *201*, 60–69, doi:10.1016/j.geomorph.2013.06.007.

Iverson, R. M. (2005), Regulation of landslide motion by dilatancy and pore pressure feedback, *J. Geophys. Res.*, *110*, F02015, doi:10.1029/2004JF000268.

Johnson, K. M., Y. Hsu, P. Segall, and S.-B. Yu (2001), Fault geometry and slip distribution of the 1999 Chi-Chi, Taiwan Earthquake imaged from inversion of GPS data, *Geophys. Res. Lett.*, *28*(11), 2285–2288, doi:10.1029/2000GL012761.

Jonsson, S., H. Zebker, P. Segall, and F. Amelung (2002), Fault slip distribution of the 1999 *Mw* 7.1 Hector Mine, California, earthquake, estimated from satellite radar and GPS measurements, *Bull. Seismol. Soc. Am.*, *92*(4), 1377–1389, doi:10.1785/0120000922.

Labazuy, P. (1996), Recurrent landslides events on the submarine flank of Piton de la Fournaise Volcano, in *Volcano Instability on the Earth and Other Planets*, *Geol. Soc. Spec. Publ.*, vol. 110, edited by W. J. McGuire, A. P. Jones, and J. Neuberg, pp. 295–306.

Le Friant, A., E. Lebas, V. Clément, G. Boudon, C. Deplus, B. De Voogd, and P. Bachèlery (2011), A new model for the evolution of La Réunion volcanic complex from complete marine geophysical surveys, *Geophys. Res. Lett.*, *38*, L09312, doi:10.1029/2011GL047489.

Lundgren, P., S. Usai, E. Sansosti, R. Lanari, M. Tesauro, G. Fornaro, and P. Berardino (2001), Modeling surface deformation observed with synthetic aperture radar interferometry at Campi Flegrei caldera, *J. Geophys. Res.*, *106*, 19,355–19,366, doi:10.1029/2001JB000194.

Lundgren, P., P. Berardino, M. Coltelli, G. Fornaro, R. Lanari, G. Puglisi, E. Sansosti, and M. Tesauro (2003), Coupled magma chamber inflation and sector collapse slip observed with synthetic aperture radar interferometry on Mt. Etna Volcano, *J. Geophys. Res.*, *108*(B5), 2247, doi:10.1029/2001JB000657.

Maerten, F., P. Resor, D. Pollard, and L. Maerten (2005), Inverting for slip on three-dimensional fault surfaces using angular dislocations, *Bull. Seismol. Soc. Am.*, *95*, 1654–1665, doi:10.1785/0120030181.

Matthews, M., and P. Segall (1993), Estimation of depth-dependent fault slip from measured surface deformation with application to the 1906 San Francisco earthquake, *J. Geophys. Res.*, *98*(B7), 12,153–12,163, doi:10.1029/93JB00440.

Meade, B. J. (2007), Algorithms for the calculation of exact displacements, strains, and stresses for triangular dislocation elements in a uniform elastic half space, *Comput. Geosci.*, *33*, 1064–1075, doi:10.1016/j.cageo.2006.12.003.

Menke, W. (2012), *Geophysical Data Analysis: Discrete Inverse Theory, Matlab edition*, 3rd ed., Academic Press.

Michon, L., and F. Saint-Ange (2008), Morphology of Piton de la Fournaise basaltic shield volcano (La Réunion Island): Characterization and implication in the volcano evolution, *J. Geophys. Res.*, *113*, B03203, doi:10.1029/2005JB004118.

Michon, L., T. Staudacher, V. Ferrazzini, P. Bachèlery, and J. Marti (2007a), April 2007 collapse of Piton de la Fournaise: A new example of caldera formation, *Geophys. Res. Lett.*, *34*, L21301, doi:10.1029/2007GL031248.

Michon, L., F. Saint-Ange, P. Bachelery, N. Villeneuve, and T. Staudacher (2007b), Role of the structural inheritance of the oceanic lithosphere in the magmato-tectonic evolution of Piton de la Fournaise Volcano (La Réunion Island), *J. Geophys. Res.*, *112*, B04205, doi:10.1029/2006JB004598.

Michon, L., V. Cayol, L. Letourneur, A. Peltier, N. Villeneuve, and T. Staudacher (2009), Edifice growth, deformation and rift zone development in basaltic setting: Insights from Piton de la Fournaise shield volcano (Réunion Island), *J. Volcanol. Geotherm. Res.*, *184*(1–2), 14–30, doi:10.1016/j.jvolgeores.2008.11.002.

Montgomery-Brown, E. K., D. K. Sinnett, M. Poland, P. Segall, T. Orr, H. Zebker, and A. Miklius (2010), Geodetic evidence for en echelon dike emplacement and concurrent slow slip during the June 2007 intrusion and eruption at Klauea Volcano, Hawaii, *J. Geophys. Res.*, *115*, B07405, doi:10.1029/2009JB006658.

Montgomery-Brown, E. K., M. P. Poland, and A. Miklius (2015), A delicate balance of magmatic-tectonic interaction at Kilauea Volcano, Hawaii, revealed from slow slip events, in *Hawaiian Volcanoes: From Source to Surface*, edited by R. Carey, pp. 269–288, John Wiley, Hoboken, N. J.

Nolesini, T., F. Di Traglia, C. Del Ventisette, S. Moretti, and N. Casagli (2013), Deformations and slope instability on Stromboli volcano: Integration of GBInSAR data and analog modeling, *Geomorphology*, *180–181*, 242–254, doi:10.1016/j.geomorph.2012.10.014.

Oehler, J.-F. (2005), Les déstabilisations de flanc des volcans de l'Ile de la Réunion (Océan Indien): Mise en évidence, implications et origines.

Okada, Y. (1985), Surface deformation due to shear and tensile faults in a half-space, *Int. J. Rock Mech. Min. Sci. Geomech. Abstr.*, *75*(4), 1135–1154, doi:10.1016/0148-9062(86)90674-1.

Okada, Y. (1992), Internal deformation due to shear and tensile faults in a half-space, *Bull. Seismol. Soc. Am.*, *82*(2), 1018–1040.

Owen, S., P. Segall, M. Lisowski, A. Miklius, R. Denlinger, and M. Sako (2000), Rapid deformation of Kilauea Volcano: Global Positioning System measurements between 1990 and 1996, *J. Geophys. Res.*, *105*(B8), 18,983–18,998, doi:10.1029/2000JB900109.

Peltier, A., T. Staudacher, and P. Bachèlery (2007), Constraints on magma transfers and structures involved in the 2003 activity at Piton de La Fournaise from displacement data, *J. Geophys. Res.*, *112*, B03207, doi:10.1029/2006JB004379.

Peltier, A., V. Famin, P. Bachèlery, V. Cayol, Y. Fukushima, and T. Staudacher (2008), Cyclic magma storages and transfers at Piton de La Fournaise Volcano (La Réunion hotspot) inferred from deformation and geochemical data, *Earth Planet. Sci. Lett.*, *270*(3–4), 180–188, doi:10.1016/j.epsl.2008.02.042.

Peltier, A., T. Staudacher, P. Bachèlery, and V. Cayol (2009a), Formation of the April 2007 caldera collapse at Piton de La Fournaise Volcano: Insights from GPS data, *J. Volcanol. Geotherm. Res.*, *184*(1–2), 152–163, doi:10.1016/j.jvolgeores.2008.09.009.

Peltier, A., P. Bachèlery, and T. Staudacher (2009b), Magma transport and storage at Piton de La Fournaise (La Réunion) between 1972 and 2007: A review of geophysical and geochemical data, *J. Volcanol. Geotherm. Res.*, *184*(1–2), 93–108, doi:10.1016/j.jvolgeores.2008.12.008.

Plattner, C., F. Amelung, S. Baker, R. Govers, and M. Poland (2013), The role of viscous magma mush spreading in volcanic flank motion at Kilauea Volcano, Hawai'i, *J. Geophys. Res. Solid Earth*, *118*, 2474–2487, doi:10.1002/jgrb.50194.

Puglisi, G., A. Bonforte, A. Ferretti, F. Guglielmino, M. Palano, and C. Prati (2008), Dynamics of Mount Etna before, during, and after the July–August 2001 eruption inferred from GPS and differential synthetic aperture radar interferometry data, *J. Geophys. Res.*, *113*, B06405, doi:10.1029/2006JB004811.

Rançon, J. P., P. Lerebour, and T. Augé (1989), The Grand Brule exploration drilling: New data on the deep framework of the Piton de la Fournaise Volcano. Part 1: Lithostratigraphic units and volcano structural implications, *J. Volcanol. Geotherm. Res.*, *36*(1–3), 113–127, doi:10.1016/0377-0273(89)90008-5.

Rossetti, F., F. Storti, and F. Salvini (2000), Cenozoic noncoaxial transtension along the Western shoulder of the Ross Sea, Antarctica, and the emplacement of McMurdo dyke arrays, *Terra Nova*, *12*(2), 60–66, doi:10.1111/j.1365-3121.2000.00270.x.

Roult, G., A. Peltier, B. Taisne, T. Staudacher, V. Ferrazzini, and A. Di Muro (2012), A new comprehensive classification of the Piton de la Fournaise activity spanning the 1985–2010 period. Search and analysis of short-term precursors from a broad-band seismological station, *J. Volcanol. Geotherm. Res.*, *241–242*, 78–104, doi:10.1016/j.jvolgeores.2012.06.012.

Sambridge, M. (1998), Exploring multidimensional landscapes without a map, *Inverse Probl.*, *14*, 427–440.

Sambridge, M. (1999a), Geophysical inversion with a neighbourhood algorithm—I. Searching a parameter space, *Geophys. J. Int.*, *138*, 479–494, doi:10.1046/j.1365-246X.1999.00876.x.

Sambridge, M. (1999b), Geophysical inversion with a neighbourhood algorithm—II. Appraising the ensemble, *Geophys. J. Int.*, *138*, 727–746, doi:10.1046/j.1365-246X.1999.00900.x.

Sigmundsson, F., et al. (2015), Segmented lateral dyke growth in a rifting event at Barðarbunga volcanic system, *Iceland, Nature*, *517*, 191–195.

Spacapan, J. B., O. Galland, H. A. Leanza, and S. Planke (2016), Control of strike-slip fault on dyke emplacement and morphology, *J. Geol. Soc. Lond.*, doi:10.1144/jgs2015-166.

Staudacher, T., V. Ferrazzini, A. Peltier, P. Kowalski, P. Boissier, P. Catherine, F. Lauret, and F. Massin (2009), The April 2007 eruption and the Dolomieu crater collapse, two major events at Piton de la Fournaise (La Réunion Island, Indian Ocean), *J. Volcanol. Geotherm. Res.*, *184*(1–2), 126–137, doi:10.1016/j.jvolgeores.2008.11.005.

Sudhaus, H., and S. Jonsson (2009), Improved source modelling through combined use of InSAR and GPS under consideration of correlated data errors: Application to the June 2000 Kleifarvatn earthquake, Iceland, *Geophys. J. Int.*, *176*(2), 389–404, doi:10.1111/j.1365-246X.2008.03989.x.

Sun, J., K. M. Johnson, Z. Cao, Z. Shen, R. Burgmann, and X. Xu (2011), Mechanical constraints on inversion of coseismic geodetic data for fault slip and geometry: Example from InSAR observation of the 6 October 2008 *Mw* 6.3 Dangxiong-Yangyi (Tibet) earthquake, *J. Geophys. Res.*, *116*, B01406, doi:10.1029/2010JB007849.

Syracuse, E. M., C. H. Thurber, C. J. Wolfe, P. G. Okubo, J. H. Foster, and B. A. Brooks (2010), High-resolution locations of triggered earthquakes and tomographic imaging of Kilauea Volcano's south flank, *J. Geophys. Res.*, *115*, B10310, doi:10.1029/2010JB007554.

Tarantola, A. (2005), *Inverse Problem Theory and Methods for Model Parameter Estimation*, Society for Industrial and Applied Mathematics, Philadelphia.

Tinard, P. (2007), *Caractérisation et modélisation des déplacements du sol associés á l'activité volcanique du Piton de la Fournaise, île de la Réunion, á partir de données interférométriques. Août 2003-Avril 2007*, PhD thesis, Université Blaise Pascal, Clermont-Ferrand.

Turcotte, D. L., and G. Schubert (2002), *Geodynamics*, 2nd ed., Cambridge Univ. Press, 456 p.

Valentine, G. A., and K. E. C. Krogh (2006), Emplacement of shallow dikes and sills beneath a small basaltic volcanic center—The role of pre-existing structure (Paiute Ridge, southern Nevada, USA), *Earth Planet. Sci. Lett.*, *246*(3–4), 217–230, doi:10.1016/j.epsl.2006.04.031.

Vlastélic, I., G. Menard, A. Gannoun, J. L. Piro, T. Staudacher, and V. Famin (2013), Magma degassing during the April 2007 collapse of Piton de la Fournaise: The record of semi-volatile trace elements (Li, B, Cu, In, Sn, Cd, Re, Tl, Bi), *J. Volcanol. Geotherm. Res.*, *254*, 97–107, doi:10.1016/j.jvolgeores.2012.12.027.

Wahba, G., and Y. Wang (1990), When is the optimal regularization parameter insensitive to the choice of the loss function? *Commun. Stat. Theory Methods*, *19*(5), 1685–1700.

Ward, S. N., and S. E. Barrientos (1986), An inversion for slip distribution and fault shape from geodetic observations of the 1983, Borah Peak, Idaho, Earthquake, *J. Geophys. Res.*, *91*(B5), 4909–4919, doi:10.1029/JB091iB05p04909.

Wauthier, C., V. Cayol, F. Kervyn, and N. D'Oreye (2012), Magma sources involved in the 2002 Nyiragongo eruption, as inferred from an InSAR analysis, *J. Geophys. Res.*, *117*, B05411, doi:10.1029/2011JB008257.

Wauthier, C., V. Cayol, M. Poland, F. Kervyn, N. D'Oreye, A. Hooper, S. Samsonov, K. Tiampo, and B. Smets (2013), Nyamulagira's magma plumbing system inferred from 15 years of InSAR, *Geol. Soc. London, Spec. Publ.*, *380*(1), 39–65, doi:10.1144/SP380.9.

Welstead, S. T. (1999), *Fractal and Wavelet Image Compression Techniques*, 232 pp., SPIE Optical Engineering Press, Bellingham, Wash.

Zeller, S. S., and D. D. Pollard (1992), Boundary conditions for rock fracture analysis using the boundary element method, *J. Geophys. Res.*, *97*(B2), 1991–1997, doi:10.1029/91JB02254.

Ziv, A., A. M. Rubin, and A. Agnon (2000), Stability of dike intrusion along preexisting fractures, *J. Geophys. Res.*, *105*(B3), 5947–5961, doi:10.1029/1999JB900410.

Zucca, J., and D. P. Hill (1980), Crustal structure of the southeast flank of Kilauea Volcano, Hawaii, from seismic refraction measurements, *Bull. Seismol. Soc. Am.*, *70*(4), 1149–1159.